Computational Mechanics
https://doi.org/10.1007/s00466-025-02721-2

ORIGINAL PAPER

Modification of solid-shell elements to suppress mesh hourglassing at bifurcation point

K. Wisniewski[1] · **E. Turska**[2]

Received: 11 July 2025 / Accepted: 7 November 2025

Abstract
The focus of a current paper is on eliminating hourglassing at the bifurcation point, particularly in simulations involving incompressible materials. Three eight-node (hexahedron) solid-shell elements that are free from the hourglassing in their tangent plane are developed for this purpose. To eliminate hourglassing, a transposition of the enhancement matrix **G** of the *Enhanced Assumed Deformation Gradient* (EADG) method is used, see Korelc and Wriggers (Eng Comput 13(1):103–123, 1996) and Glaser and Armero (Eng Comput 14(7):759–791, 1997). Several modifications are proposed to convert three existing (parent) solid-shell elements into the new ones: 1. A two-parameter enhancement (EADG2) of the deformation gradient **F** is proposed to suppress hourglassing of our *Hu–Washizu* element HW19 and the *Enhanced Assumed Strain* element EAS10. Originally neither of them uses the EADG method, so they are reformulated to embed it. 2. A new transformation rule (designated T4) is proposed for the EADG enhancement, and it involves the inverse of the current Jacobian for large deformations. T4 is an alternative to the other three transformations used in the literature. We check that T4 is objective and subject it to numerical tests in the current paper. 3. For the third parent element, which uses the standard EADG4 enhancement, we propose 3 additional modes, which are necessary to eliminate one of the large spurious eigenvalues for the nearly incompressible material and to improve its bending behavior. The improved performance of the obtained elements is demonstrated using several linear and non-linear examples for the linear elastic material and the neo-Hookean hyperelastic material. They are also compared to the best existing solid-shell elements.

Keywords Shell · Finite element · Instability · Finite deformation · Bifurcation

1 Introduction

The 8-node hexahedron solid-shell elements have already achieved a considerable level of maturity and are applied to analyze shell structures at finite strains. For shell structures, especially in bending dominated problems, they outperform the 8-node 3D solid elements, partly due to adaptation of techniques developed for shell elements that eliminate various types of locking. In our recent paper Wisniewski and Turska [52] on the *reduced representation* Hu–Washizu (HW) solid-shell elements, several formulations of these elements are tested and compared.

Solid-shell elements play an important role in structural analysis of multi-layer composites because nodes located at bounding surfaces allow for straightforward aggregation of layers. They form the basis of more advanced and numerically effective shell models of composites, see, e.g., [13–17, 45].

Although inelasticity remains beyond the scope of present work we would like to mention several papers including elasto-plasticity for solid-shells, see, e.g., [11, 19, 20, 37, 38]. Solid-shells not only require the adaptation of the 3D or plane stress constitutive algorithms but also the inclusion of additional methods, such as the *Assumed Natural Strain* (ANS) method.

Mesh hourglassing of solid elements In Simo and Armero [39], the hourglass patterns of the mesh for the element Q1/P0, which is based on the mean dilatation approach of Nagtegaal et al. [29], are attributed to a failure of the

✉ K. Wisniewski
kwisn@ippt.pan.pl

[1] IFTR, Polish Academy of Sciences, Pawińskiego 5B, 02-106 Warsaw, Poland

[2] Polish Japanese Academy of Information Technology, Koszykowa 86, 02-008 Warsaw, Poland

Published online: 26 November 2025

LBB condition. The presence of undesirable modes at high strains for the enhanced 2D plane strain 4-node element Q1/E4 is noted in that paper, but not analyzed.

A simple 2D example that can be solved analytically and also exhibits hourglassing was first proposed by Wriggers and Reese [56]. They analyzed a single enhanced 2D plane strain 4-node element, which resulted in analytical expressions and plots of the eigenvalues as functions of the stretch. For compressible neo-Hookean material with Lamé constants $\Lambda = 10^5$ and $\mu = 20$ (for which $\nu = 0.499975$), the critical stretch $\lambda_2 = 0.6116$ and the hourglassing mode were obtained. It was observed that for the standard (non-enhanced) element, no singularity appears for physically meaningful values of Lamé constants ($\Lambda \geq 0,\ \mu > 0$) thus a singular point is a result of the enhancement.

This problem subsequently was analyzed further in Korelc and Wriggers [25], Wriggers and Korelc [55], Glaser and Armero [12] and Armero [3]. It was found for the Ogden material that hourglassing is also possible under tension [12]. Several other very good papers were published, e.g., [3, 8, 9, 30, 31, 35], to mention the early ones. A comprehensive overview is provided in Wriggers [54, Sect. 10].

Several methods of controlling the spurious modes were devised, and the simplest one is the method of transposition of the matrix $\mathbf{G}$ of the *Enhanced Assumed Deformation Gradient* (EADG) enhancement proposed in Korelc and Wriggers [25] and Glaser and Armero [12]. Other methods use hourglass stabilization with user-defined parameters, see [2, 12], or hourglass stabilization based on mixed methods, see [36, 46]. In the current paper, we use the method of transposition of $\mathbf{G}$.

In passing we note that to remove mild spurious deformation modes, the governing functional can be supplemented by the penalty term $\int_B \frac{1}{2}\beta\ [\det(\mathbf{I} + \widetilde{\mathbf{F}}) - 1]^2\ dV$. This term constrains the volume changes due to the enhancement of deformation gradient $\widetilde{\mathbf{F}}$, see [12, Eq. (29)] and [24, p. 656]. The penalty number β can be used as the stabilization parameter. An additional constraint on the enhancement was earlier used in [30], and it required the variation of the enhancing field to be orthogonal to a piece-wise constant pressure field. In consequence, the instantaneous rate of change of the volume due to solely the enhancing field is zero when the nodal positions are held fixed.

Recently, Pfefferkorn and Betsch [33] developed a 3D solid element based on the Petrov-Galerkin method with the enhancement of the spatial displacement gradient $\partial \mathbf{u}(\mathbf{X})/\partial \mathbf{x} = \mathbf{I} - \mathbf{F}^{-1}$ instead of the deformation gradient $\mathbf{F}$, where $\mathbf{X}$ and $\mathbf{x}$ are the initial and current position vectors, respectively. This element eliminates the spurious hourglass instabilities but uses an unsymmetric stiffness matrix.

Mesh hourglassing of solid-shell elements The currently used 8-node solid-shell elements stem from the earlier developed 3D solid elements; we elaborated on this relation in [52]. They use the same interpolation functions and constitutive modules, but the solid-shell elements also use additional specialized methods to pass the bending patch test and to improve their behavior in thin shell applications involving bending/twisting dominated problems.

1. The *0th order* thickness strain is improperly approximated for curved or trapezoidal through-thickness shape of elements (deformed or undeformed) causing the so-called curvature thickness locking. The *Assumed Natural Strain* (ANS) method proposed in Betsch and Stein [5] is used to circumvent this issue.
2. The out-of-plane bending is impaired by the zero value of the *1st order* thickness strain, which causes the volumetric (or dilatational or Poisson's ratio or Poisson's thickness) locking. To remedy this problem, this strain is enhanced using the EAS method, see Büchter et al. [6], Vu-Quoc and Tan [44] and our [52]. Also a specific representation of the assumed thickness strain in the HW elements can be used, see Klinkel et al. [23].
3. To reduce the transverse shear locking, the ANS method proposed by Dvorkin and Bathe [10] is applied to the *0th order* transverse shear strains.

These methods significantly improve behavior of the 8-node solid-shell elements, and for this reason are indispensable in this class of elements.

We note that hourglassing at the bifurcation point is not recognized as a problem in the existing literature on the solid-shell elements, and our recent paper [52] on the *reduced representation* HW solid-shell elements seems to be an exception.

For shell structures modeled by solid-shell elements, the loss of stability can be caused by the element's formulation and also by structural design. To check the solid-shell element's formulation, the test should exclude the latter cause, as, e.g., the "Compression of a nearly-incompressible block" test of Sect. 5.3.4. We performed this test in our recent paper [52], and all of the tested and reference solid-shell elements exhibited mesh hourglassing, see Table 12 therein. This provides a strong motivation to develop the solid-shell elements that are free of hourglassing under tangent compression.

Objectives of the current paper The focus of a current paper is on eliminating hourglassing at the bifurcation point, particularly in simulations involving solid-shell elements and the nearly incompressible hyperelastic material. (We stress that this paper is not on suppressing the hourglassing caused by reduced integration.) The applied

method to suppress mesh hourglassing utilizes a transposition of the matrix $\mathbf{G}$ of the *Enhanced Assumed Deformation Gradient* (EADG) enhancement as proposed in Korelc and Wriggers [25] and Glaser and Armero [12].

1. To obtain new hourglassing-free elements we will modify two existing solid-shell elements, our *Hu–Washizu* element HW19 [52] and the *Enhanced Assumed Strain* element EAS10 (see Sect. 4.2.1), which are both based on Green strain/2nd Piola-Kirchhoff stress, and treated as the parent elements.
   These two elements are stable and pass the membrane/bending patch tests. They have one large eigenvalue for nearly-incompressible material ($\nu = 0.4999999999$), and yield quite accurate results in benchmark tests. However, they produce hourglassing of the mesh at the bifurcation strain for the nearly-incompressible material. In the current paper, we will improve these elements to make them resilient to this type of hourglassing.
2. Elements HW19 and EAS10 do not use the EADG enhancement so we propose to extend their governing functionals and incorporate an enhancement of the deformation gradient $\mathbf{F}$. The basic ideas pertaining to the EADG enhancement are as follows:

   (A) Regarding the assumed representation, it was noticed in [25] and [12] for 2D plane strain elements and the standard 4-parameter representation EADG4 defined as

$$\mathbf{G}(q_i,\ \xi,\eta) \doteq \begin{bmatrix} q_1\xi & q_3\eta \\ q_4\xi & q_2\eta \end{bmatrix}, \quad i = 1,\dots,4, \tag{1}$$

   that a transposition of this $\mathbf{G}$ suppresses the mesh hourglassing. Here $\xi,\eta \in [-1,+1]$ are natural coordinates. Since the transposition affects only the off-diagonal terms of EADG4, we propose to use a simpler 2-parameter representation EADG2,

$$\mathbf{G}(q_i,\ \xi,\eta) \doteq \begin{bmatrix} 0 & q_1\eta \\ q_2\xi & 0 \end{bmatrix}, \quad i = 1,2, \tag{2}$$

   in the new solid-shell elements. For the version of EADG2 used in our solid-shell elements, see Eq. (47).

   (B) Regarding the transformation rules for the EADG enhancement, three such rules can be found in the literature: T1 by Simo et al. [40], T2 by Glaser and Armero [12], and T3 by Pfefferkorn and Betsch [32], where the designations T1, T2 and T3 are introduced here for brevity. In the current paper, we propose a new transformation rule, designated T4, which for large deformations involves $(\mathbf{J}_0^{\text{curr}})^{-T}$, where $\mathbf{J}_0^{\text{curr}}$ is the current Jacobian at the element's center. T4 is tested with the 2-parameter $\mathbf{G}$ and its transpose.
3. We will also modify the third existing solid-shell element, designated EADG4, in which the EADG4 enhancement of the membrane strains suffices to suppress the mesh hourglassing. Unfortunately, this element has two large eigenvalues for the nearly incompressible hyperelastic material. Therefore, we have introduced 3 additional modes, to obtain the EADG7 representation, which eliminates one of these large eigenvalues and improves the element's bending behavior.
4. The three new solid-shell elements are tested against the two reference solid-shell elements, which are currently considered as the best in this class: the HSEE element of Klinkel et al. [23] and the EAS10 element, which is characterized in Sect. 4.2.1. Several other elements are also used for comparison, including a 3D solid element and the Reissner-Mindlin's shell elements with 6 dofs/node. Comparison to the *reduced representation* HW solid-shell elements of our recent paper [52] can also be made.
   The performance of the developed solid-shell elements is demonstrated using several linear and non-linear examples for the linear elastic material and the incompressible hyper-elastic material. The accuracy of solutions, the convergence properties of the Newton method and the mesh hourglassing in the large strain compression are examined.

Outline of the paper The outline of the paper is as follows: the general characteristics of the solid-shell elements are provided in Sect. 2, which includes the ANS methods for the thickness and transverse shear strains in Sect. 2.1. The enhancement of the deformation gradient is described and analyzed in Sect. 3; the transformation rules for the EADG enhancement are in Sect. 3.1 and the assumed representation EADG2 in Sect. 3.2.

New solid-shell elements are presented in Sect. 4, which includes the HW element with EADG2 enhancement in Sect. 4.1, the EAS element with EADG2 enhancement in Sect. 4.2 and, finally, the EADG7 element in Sect. 4.3. Numerical tests in Sect. 5 demonstrate the performance of the developed hourglassing-free solid-shell elements. The paper concludes with final remarks in Sect. 6.

Notation: "parameter" is abbreviated to "p". As for the components, "COV" stands for "covariant", "CTV" for "contravariant" and "CART" for "Cartesian". The elemental parameters are denoted as q_i, $i = 1,\dots,N_q$, and the vector of these parameters as $\mathbf{q}$.

2 General characteristics of solid-shell elements

This section first provides the general characteristics of the solid-shell 8-node elements. Next, their kinematics is described.

Basic definitions for solid-shell element. Consider a 8-node isoparametric solid-shell element with the nodes numbered as shown in Fig. 1. The nodal "directors" are defined as the vectors linking the corresponding nodes at the bottom and top surfaces, i.e. 1–5, 2–6, 3–7 and 4–8. They can by non-parallel and not perpendicular to the element's middle surface, which can be either flat or warped, similarly to the middle surface of the Reissner-Mindlin's 4-node shell elements, see e.g. [48]. The reference elemental basis is designated as $\{\mathbf{i}_k\}$, $(k = 1, 2, 3)$.

The following vectors are associated with the solid-shell element: the initial position $\mathbf{X}$, the displacement $\mathbf{u}$ and the current position $\mathbf{x}$. The first two vectors are interpolated as follows:

$$\begin{aligned} \mathbf{X}(\xi,\eta,\zeta) &= \sum_{I=1}^{8} N_I(\xi,\eta,\zeta)\ \mathbf{X}_I, \\ \mathbf{u}(\xi,\eta,\zeta) &= \sum_{I=1}^{8} N_I(\xi,\eta,\zeta)\ \mathbf{u}_I, \end{aligned} \tag{3}$$

where the standard tri-linear shape functions are

$$N_I(\xi,\eta,\zeta) \doteq \sum_{I=1}^{8} \frac{1}{8}(1+\xi_I\xi)(1+\eta_I\eta)(1+\zeta_I\zeta), \tag{4}$$

$\xi,\eta,\zeta \in [-1,+1]$ are the natural coordinates and $\{\xi_I,\eta_I,\zeta_I\} = \{\pm1,\pm1,\pm1\}$ are the natural coordinates of nodes $I = 1,\ldots,8$. The current position $\mathbf{x}$ is obtained as $\mathbf{x}(\xi,\eta,\zeta) \doteq \mathbf{X}(\xi,\eta,\zeta) + \mathbf{u}(\xi,\eta,\zeta)$.

The thickness vector is defined as $\mathbf{h}(\xi,\eta) \doteq \mathbf{X}(\xi,\eta,\zeta=1) - \mathbf{X}(\xi,\eta,\zeta=-1)$ and the ζ -coordinate is associated with it. The reference (middle) surface is at $\zeta = 0$ while the bounding top/bottom surfaces at $\zeta = \pm1$. Note that for solid-shells the "thickness" is defined as $h \doteq \|\mathbf{h}\|$, i.e. differently than the thickness for the Reissner-Mindlin's shells.

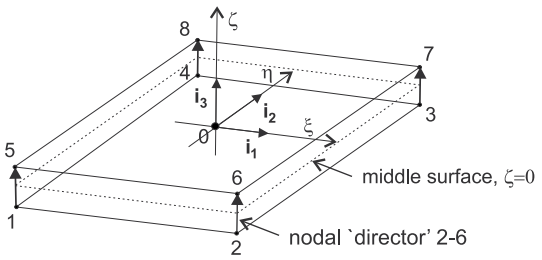

Fig. 1 Numbering of nodes and the reference elemental basis $\{\mathbf{i}_k\}$ of 8-node solid-shell element. ζ is the thickness coordinate

Jacobian matrix Let us denote the components of the initial position vector $\mathbf{X}$ in the global reference Cartesian basis $\{\mathbf{e}_k\}$ as X_k $(k = 1, 2, 3)$. The Jacobian matrix is defined as

$$\mathbf{J} \doteq \left[\frac{\partial X_k}{\partial \xi^l}\right] = \begin{bmatrix} \mathbf{g}_1\cdot\mathbf{i}_1 & \mathbf{g}_2\cdot\mathbf{i}_1 & \mathbf{g}_3\cdot\mathbf{i}_1 \\ \mathbf{g}_1\cdot\mathbf{i}_2 & \mathbf{g}_2\cdot\mathbf{i}_2 & \mathbf{g}_3\cdot\mathbf{i}_2 \\ \mathbf{g}_1\cdot\mathbf{i}_3 & \mathbf{g}_2\cdot\mathbf{i}_3 & \mathbf{g}_3\cdot\mathbf{i}_3 \end{bmatrix}, \tag{5}$$

where $\xi^l \doteq \{\xi,\eta,\zeta\}_l$ $(l = 1, 2, 3)$. The vectors of the natural basis $\{\mathbf{g}_l\}$ in the initial configuration are defined as $\mathbf{g}_l \doteq \partial\mathbf{X}/\partial\xi_l$. The vectors $\mathbf{i}_k$ of the elemental Cartesian basis at the element's center $\{\mathbf{i}_k\}$ are constructed in the standard way, see e.g. [52, Eqs. (6)–(9)].

The matrix in Eq. (5) is obtained from the equation $(X_k - X_{0k})\ \mathbf{i}_k = \xi^l\ \mathbf{g}_l$, where X_{0k} are components of the position vector of the element's center $\mathbf{X}_0$. Differentiating both sides of this equation w.r.t. ξ^l and taking a scalar product with $\mathbf{i}_k$, we obtain $\partial X_k/\partial\xi^l = \mathbf{g}_l\cdot\mathbf{i}_k$.

Note that if $\mathbf{X}$ is replaced by $\mathbf{X}^* = \mathbf{R}^T(\mathbf{X} - \mathbf{X}_0)$, where $\mathbf{R} \in \mathrm{SO}(3)$ is a rotation, then $\mathbf{g}_l^* \doteq \partial\mathbf{X}^*/\partial\xi^l = \mathbf{R}^T\mathbf{g}_l$ and $\mathbf{i}_k^* = \mathbf{R}^T\mathbf{i}_k$ on use of $\mathbf{g}_\alpha^*$ in place of $\mathbf{g}_\alpha$ $(\alpha = 1, 2)$ in Eqs. (6)–(9) of [52]. Then $\mathbf{g}_l^*\cdot\mathbf{i}_k^* = \mathbf{g}_l\cdot\mathbf{i}_k$, and $\partial X_k^*/\partial\xi^l = \partial X_k/\partial\xi^l$ follows. Hence $\mathbf{J}$ is invariant to the $\mathbf{R}^T(\mathbf{X} - \mathbf{X}_0)$ transformation, which can be used in the element's formulation.

Kinematics of solid-shells. The configuration space of the Cauchy continuum is defined as: $\mathcal{C} \doteq \{\boldsymbol{\chi}\colon\ B \to R^3\}$, where B is the reference configuration of the body. The deformation function $\boldsymbol{\chi}\colon\ \mathbf{x} = \boldsymbol{\chi}(\mathbf{X})$ maps the reference (non-deformed) configuration onto the current (deformed) one. The deformation gradient is defined as

$$\mathbf{F} \doteq \frac{\partial\mathbf{x}}{\partial\mathbf{X}}, \tag{6}$$

where $\mathbf{X}$ is the position vector in the initial (non-deformed) configuration and $\mathbf{x}$ is the position vector in the current (deformed) one. Using the convective coordinates $\boldsymbol{\xi} \doteq \{\xi,\eta,\zeta\}$, we can parameterize the position vectors as $\mathbf{X}(\boldsymbol{\xi})$ and $\mathbf{x}(\boldsymbol{\xi})$. For the components in the Cartesian reference basis $\{\mathbf{i}_k\}$, we obtain

$$\mathbf{F} \doteq \frac{\partial\mathbf{x}}{\partial\mathbf{X}} = \frac{\partial\mathbf{x}}{\partial\boldsymbol{\xi}}\frac{\partial\boldsymbol{\xi}}{\partial\mathbf{X}} = \mathbf{J}^{\mathrm{curr}}\,\mathbf{J}^{-1}, \tag{7}$$

where $\mathbf{J}^{\mathrm{curr}} \doteq \partial\mathbf{x}/\partial\boldsymbol{\xi}$ and $\mathbf{J} \doteq \partial\mathbf{X}/\partial\boldsymbol{\xi}$ are the current and initial Jacobians, respectively. Note that $\mathbf{J}^{\mathrm{curr}}$ is related to $\mathbf{J}$ by the gradient of displacements, i.e.

$$\mathbf{J}^{\mathrm{curr}} = \frac{\partial \mathbf{x}}{\partial \boldsymbol{\xi}} = \frac{\partial (\mathbf{X} + \mathbf{u})}{\partial \boldsymbol{\xi}} = \mathbf{J} + \frac{\partial \mathbf{u}}{\partial \boldsymbol{\xi}}. \tag{8}$$

The Green strain is defined as

$$\mathbf{E} \doteq \frac{1}{2}\left(\mathbf{F}^T\mathbf{F} - \mathbf{I}\right) \quad \text{or} \quad \mathbf{E} \doteq \mathbf{J}^{-T}\ \mathbf{E}^{\mathrm{COV}}\ \mathbf{J}^{-1}, \tag{9}$$

where the covariant (COV) components are computed as either

$$\begin{aligned} \mathbf{E}^{\mathrm{COV}} &= \frac{1}{2}\left[(\mathbf{J}^{\mathrm{curr}})^T\ \mathbf{J}^{\mathrm{curr}} - \mathbf{J}^T\ \mathbf{J}\right] \\ \text{or} \quad E_{ij}^{\mathrm{COV}} &= \frac{1}{2}\left(\bar{\mathbf{g}}_i \cdot \bar{\mathbf{g}}_j - \mathbf{g}_i \cdot \mathbf{g}_j\right), \end{aligned} \tag{10}$$

where $\bar{\mathbf{g}}_1 \doteq \partial\mathbf{x}/\partial\xi$, $\bar{\mathbf{g}}_2 \doteq \partial\mathbf{x}/\partial\eta$ and $\bar{\mathbf{g}}_3 \doteq \partial\mathbf{x}/\partial\zeta$ are vectors of the natural basis $\{\bar{\mathbf{g}}_i\}$ in the deformed (current) configuration. Besides $i, j = 1, 2, 3$.

For the solid-shell elements, we linearly expand the strain $\mathbf{E}$ in the thickness coordinate ζ at the reference surface $\zeta = 0$ as follows:

$$\mathbf{E}(\zeta) \approx \mathbf{E}^0 + \zeta\ \mathbf{E}^1, \quad \zeta \in [-1, +1], \tag{11}$$

where the *0th* and the *1st order* strains are defined as

$$\mathbf{E}^0 \doteq \mathbf{E}(\zeta)|_{\zeta=0}, \qquad \mathbf{E}^1 \doteq \left.\frac{\partial \mathbf{E}(\zeta)}{\partial \zeta}\right|_{\zeta=0}. \tag{12}$$

The *0th* and *1st order* parts of strain are designated by the superscript "0" and "1", respectively.

2.1 Treatment of transverse shear and thickness strains

In this section we discuss specialized methods used to improve the transverse shear strain and the thickness strain. A full description of our implementation of these methods is given in [52, Sect. 4].

1. The ANS method in the form proposed in Dvorkin and Bathe [10] is applied to transverse shear strains $E_{3\alpha}^0$ to reduce the transverse shear locking.

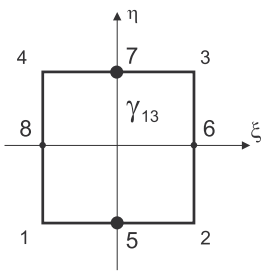

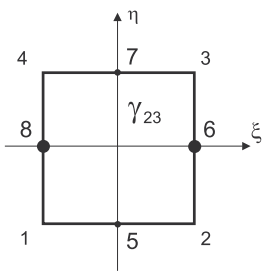

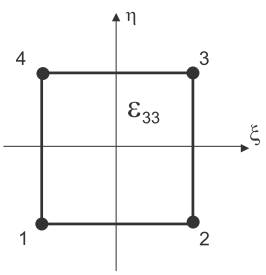

Fig. 2 ANS method. Location of sampling points for γ_{13},γ_{23} and ε_{33} at $\zeta = 0$

Let us denote the covariant components of the transverse shear strains at the reference surface $\zeta = 0$ by $\gamma_{\alpha 3} \doteq 2E_{\alpha 3}^{0\ \mathrm{COV}}$ $(\alpha = 1, 2)$, and proceed as follows. First, values of $\gamma_{\alpha 3}$ are computed (sampled) at the middle points of element sides, and denoted by γ_{13}^7, γ_{13}^5 for $(\xi = 0,\ \eta = \pm 1)$ and γ_{23}^6, γ_{23}^8 for $(\xi = \pm 1,\ \eta = 0)$, see Fig. 2. Next, $\gamma_{\alpha 3}$ are interpolated linearly in one direction using the sampled values as follows:

$$\begin{aligned} \widetilde{\gamma}_{13}(\xi, \eta) &= \frac{1}{2}\left[(1 - \eta)\ \gamma_{13}^5 + (1 + \eta)\ \gamma_{13}^7\right], \\ \widetilde{\gamma}_{23}(\xi, \eta) &= \frac{1}{2}\left[(1 - \xi)\ \gamma_{23}^6 + (1 + \xi)\ \gamma_{23}^8\right]. \end{aligned} \tag{13}$$

2. The ANS method in the form proposed by in Betsch and Stein [5] is applied to the thickness strain E_{33}^0 to circumvent the thickness straining appearing in bending for trapezoidal through-thickness shapes of the element, i.e. when the nodal "directors" are non-parallel.

We denote the covariant thickness strain at the reference surface $\zeta = 0$ by $\varepsilon_{33} \doteq E_{33}^{0\ \mathrm{COV}}$, and proceed as follows. First, ε_{33} is computed (sampled) at 4 corner points $(\xi = \pm 1,\ \eta = \pm 1)$, see Fig. 2, and denoted as $(\varepsilon_{33})_I$, $I = 1, 2, 3, 4$. Next, ε_{33} is interpolated within an element using the bi-linear shape functions $N_I(\xi, \eta)$,

$$\widetilde{\varepsilon}_{33}(\xi, \eta) = \Sigma_{I=1}^4\ N_I(\xi, \eta)\ (\varepsilon_{33})_I. \tag{14}$$

Finally, the ANS modified strains of Eqs. (14) and (13) are transformed to the Cartesian components

$$\mathbf{E}_{\mathrm{v}}^{0\ \mathrm{CART}} = (\mathbf{T}_{\mathrm{S}}^0)^{-T}\ \left[0, 0, \widetilde{\varepsilon}_{33},\ 0, \widetilde{\gamma}_{13}, \widetilde{\gamma}_{23}\right]^T, \tag{15}$$

where $\mathbf{T}_{\mathrm{S}}^0$ is computed at the element's center. The strain vector $\mathbf{E}_{\mathrm{v}}$ and the operator $\mathbf{T}_{\mathrm{S}}$ are defined in Appendix 1. Alternatively,

$$\begin{aligned} &\mathbf{E}^{0\ \mathrm{CART}} = \mathbf{J}_0^{-T}\ \mathbf{E}^{0\ \mathrm{COV}}\ \mathbf{J}_0^{-1}, \quad \text{where} \\ &\mathbf{E}^{0\ \mathrm{COV}} \doteq \begin{bmatrix} 0 & 0 & \widetilde{\gamma}_{13}/2 \\ & 0 & \widetilde{\gamma}_{23}/2 \\ \text{sym.} & & \widetilde{\varepsilon}_{33} \end{bmatrix}. \end{aligned} \tag{16}$$

3. The *1st order* thickness strain E_{33}^1 is equal to zero, and it is introduced using the *Enhanced Assumed Strain* (EAS) method

$$\mathbf{E}_{\mathrm{v}}^{1\,\mathrm{EAS}} = (\mathbf{T}_{\mathrm{S}}^{0})^{-T}\ [0,0,\mathrm{G}_{33}^{1\,\mathrm{COV}},\ 0,0,0]^{T}\ \frac{j_0}{j}, \tag{17}$$

where $\mathrm{G}_{33}^{1\,COV} \doteq (q_1 + q_2\xi + q_3\eta)\,\zeta$ and it depends on the thickness coordinate ζ. Alternatively,

$$\mathbf{E}^{1\,\mathrm{EAS}}(\mathbf{u},\mathbf{q}) \ = \ \mathbf{J}_0^{-T}\ \mathbf{G}^1(\mathbf{q})\ \mathbf{J}_0^{-1}\ \frac{j_0}{j}, \tag{18}$$

where

$$\mathbf{G}^1(q_i,\ \xi,\eta,\zeta) \doteq \begin{bmatrix} 0 & 0 & 0 \\ 0 & 0 & 0 \\ 0 & 0 & \mathrm{G}_{33}^{1\,\mathrm{COV}} \end{bmatrix}, \quad i = 1,\ldots,3. \tag{19}$$

The transverse shear strain and the thickness strain are treated as described above in all the solid-shell elements described in Sect. 4.

3 Enhancement of the deformation gradient

In this section, we consider different forms of the enhancement of deformation gradient for finite deformations. A new transformation rule, designated T4, which is different than those existing in the literature, is proposed.

The *Enhanced Assumed Displacement Gradient* (EADG) method was proposed for 2D plane strain elements in Simo and Armero [39]. It is a generalization of the *Incompatible Displacement* (ID) method of Wilson et al. [47] and Taylor et al. [42]. However, the enhancement is not the gradient of an incompatible displacement field and continuity across element boundaries is not required. This has the consequences discussed, e.g., in Nagtegaal and Fox [30]. The EADG method is based on the additive enhancement of the deformation gradient $\mathbf{F}(\mathbf{u})$,

$$\mathbf{F}^{\mathrm{enh}}(\mathbf{u},\mathbf{q}) \ = \ \underbrace{\mathbf{F}(\mathbf{u})}_{\text{for compatible } \mathbf{u}} \ + \ \underbrace{\mathbf{H}(\mathbf{u},\mathbf{G}(\mathbf{q},\boldsymbol{\xi}))}_{\text{enhancement}}, \tag{20}$$

where $\mathbf{u}$ is the vector of compatible displacements, $\mathbf{q}$ is the vector of additional (elemental) parameter, $\mathbf{H}$ is the matrix of enhancement and $\mathbf{G}(\mathbf{q},\boldsymbol{\xi})$ is a matrix of assumed representations.

3.1 Transformations for enhancement H

Below we discuss four transformation rules, designated T1, T2, T3 and T4, which are used to define the enhancement $\mathbf{H}$. The dependence of $\mathbf{H}$ on $\mathbf{u}$ and $\boldsymbol{\xi}$ is not indicated.

Transformation T1 For large deformations, the enhancement $\mathbf{H}$ is defined in Simo et al. [40] by Eqs. (3.4) and (3.6), which, in the current notation, is

$$\mathbf{H}(\mathbf{q}) = \mathbf{F}_0\ \widetilde{\mathbb{F}1}(\mathbf{q}), \tag{21}$$

where the enhancement for small deformations is

$$\widetilde{\mathbb{F}1}(\mathbf{q}) = \mathbf{J}_0\ \mathbf{G}(\mathbf{q})\ \mathbf{J}_0^{-1}\frac{j_0}{j}. \tag{22}$$

Besides $j \doteq \det \mathbf{J}$, and at the element's center $j_0 \doteq j(\boldsymbol{\xi}_0)$. The above formula contains the "MIX1 → CART"transformation of Table 1. Inserting Eq. (22) into Eq. (21), we obtain

$$\mathbf{H}(\mathbf{q}) = \underline{\mathbf{F}_0\,\mathbf{J}_0}\ \mathbf{G}(\mathbf{q})\ \mathbf{J}_0^{-1}\frac{j_0}{j} \ = \ \mathbf{J}_0^{\mathrm{curr}}\ \mathbf{G}(\mathbf{q})\ \mathbf{J}_0^{-1}\frac{j_0}{j}, \tag{23}$$

where from Eq. (7), we obtain $\mathbf{F}_0\,\mathbf{J}_0 = \mathbf{J}_0^{\mathrm{curr}}$, i.e. the current Jacobian at the element's center. From Eq. (8), $\mathbf{J}_0^{\mathrm{curr}}$ is related to $\mathbf{J}_0$ by the gradient of displacements at the element's center, i.e.

$$\mathbf{J}_0^{\mathrm{curr}} = \mathbf{J}_0\ + \left(\frac{\partial \mathbf{u}}{\partial \boldsymbol{\xi}}\right)_0. \tag{24}$$

Hence, for small deformations, when $(\partial\mathbf{u}/\partial\boldsymbol{\xi})_0 \approx \mathbf{0}$, we have $\mathbf{J}_0^{\mathrm{curr}} \approx \mathbf{J}_0$.

Transformation T2 Another form of $\mathbf{H}$ is proposed in Korelc and Wriggers [25, Eq. (13)] and Glaser and Armero [12, Eq. (4)]. For large deformations, $\mathbf{H}$ of Eq. (21) is still used but the enhancement for small deformations is defined as

Table 1 Summary of transformations of components of the 2nd rank tensor $\mathbf{A}$

Transformation	Formula
CTV → CART	$\mathbf{A}^{\mathrm{CART}} = \mathbf{J}\ \mathbf{A}^{\mathrm{CTV}}\ \mathbf{J}^{T}$
COV → CART	$\mathbf{A}^{\mathrm{CART}} = (\mathbf{J}^{-1})^{T}\ \mathbf{A}_{\mathrm{COV}}\ \mathbf{J}^{-1}$
MIX1 → CART	$\mathbf{A}^{\mathrm{CART}} = \mathbf{J}\ \mathbf{A}^{\mathrm{MIX1}}\ \mathbf{J}^{-1}$
MIX2 → CART	$\mathbf{A}^{\mathrm{CART}} = (\mathbf{J}^{-1})^{T}\ \mathbf{A}^{\mathrm{MIX2}}\ \mathbf{J}^{T}$

$$\widetilde{\mathbb{F}2}(\mathbf{q}) = \mathbf{J}_0^{-T}\ \mathbf{G}(\mathbf{q})\ \mathbf{J}_0^{-1}\frac{j_0}{j}. \tag{25}$$

The above formula contains the "COV → CART"transformation of Table 1. Combining Eqs. (21) and (25) together, we have

$$\begin{aligned}\mathbf{H}(\mathbf{q}) &= \underline{\mathbf{F}_0\,\mathbf{J}_0^{-T}}\ \mathbf{G}(\mathbf{q})\ \mathbf{J}_0^{-1}\frac{j_0}{j}\\ &= \mathbf{J}_0^{\text{curr}}\left(\mathbf{J}_0^T\mathbf{J}_0\right)^{-1}\mathbf{G}(\mathbf{q})\ \mathbf{J}_0^{-1}\frac{j_0}{j},\end{aligned} \tag{26}$$

where $\mathbf{F}_0 = \mathbf{J}_0^{\text{curr}}\mathbf{J}_0^{-1}$ by Eq. (7) and $\left(\mathbf{J}_0^{-1}\mathbf{J}_0^{-T}\right) = \left(\mathbf{J}_0^T\mathbf{J}_0\right)^{-1}$. For small deformations $\mathbf{J}_0^{\text{curr}} \approx \mathbf{J}_0$, and then $\mathbf{J}_0^{\text{curr}}\left(\mathbf{J}_0^{-1}\mathbf{J}_0^{-T}\right) \approx \mathbf{J}_0^{-T}$.

Transformation T3 Another form of $\mathbf{H}$ is proposed in Pfefferkorn and Betsch [32, Eq. (35)], and $\mathbf{F}_0$ in transformation T1 is replaced by $\mathbf{F}_0^{-T}$, i.e.

$$\mathbf{H}(\mathbf{q}) = \mathbf{F}_0^{-T}\ \widetilde{\mathbb{F}1}(\mathbf{q}). \tag{27}$$

Using $\widetilde{\mathbb{F}1}$ of Eq. (22), we obtain

$$\begin{aligned}\mathbf{H}(\mathbf{q}) &= \underline{\mathbf{F}_0^{-T}\,\mathbf{J}_0}\ \mathbf{G}(\mathbf{q})\ \mathbf{J}_0^{-1}\frac{j_0}{j}\\ &= \ (\mathbf{J}_0^{\text{curr}})^{-T}\left(\mathbf{J}_0^T\,\mathbf{J}_0\right)\ \mathbf{G}(\mathbf{q})\ \mathbf{J}_0^{-1}\frac{j_0}{j},\end{aligned} \tag{28}$$

where $\mathbf{F}_0^{-T} = (\mathbf{J}_0^{\text{curr}})^{-T}\mathbf{J}_0^T$ by Eq. (7). Note that $\left(\mathbf{J}_0^T\,\mathbf{J}_0\right)$ appears in the above formula while its inverse in Eq. (26). For small deformations $\mathbf{J}_0^{\text{curr}} \approx \mathbf{J}_0$, and we obtain $(\mathbf{J}_0^{\text{curr}})^{-T}\left(\mathbf{J}_0^T\,\mathbf{J}_0\right) \approx \mathbf{J}_0$.

Transformation T4 In the current paper, we propose another transformation rule for large deformations, i.e.

$$\mathbf{H}(\mathbf{q}) = \mathbf{F}_0^{-T}\ \widetilde{\mathbb{F}2}(\mathbf{q}), \tag{29}$$

where $\mathbf{F}_0^{-T}$ is used instead of $\mathbf{F}_0$, when compared to Eq. (21). Using $\widetilde{\mathbb{F}2}(\mathbf{q})$ of Eq. (25) in the above formula, we obtain

$$\begin{aligned}\mathbf{H}(\mathbf{q}) &= \underline{\mathbf{F}_0^{-T}\,\mathbf{J}_0^{-T}}\ \mathbf{G}(\mathbf{q})\ \mathbf{J}_0^{-1}\ \frac{j_0}{j}\\ &= (\mathbf{J}_0^{\text{curr}})^{-T}\ \mathbf{G}(\mathbf{q})\ \mathbf{J}_0^{-1}\ \frac{j_0}{j},\end{aligned} \tag{30}$$

where $\mathbf{F}_0^{-T}\mathbf{J}_0^{-T} = (\mathbf{F}_0\,\mathbf{J}_0)^{-T} = (\mathbf{J}_0^{\text{curr}})^{-T}$. For small deformations $(\mathbf{J}_0^{\text{curr}})^{-T} \approx \mathbf{J}_0^{-T}$.

In summary, the above described four transformation rules are as follows:

$$\begin{aligned}
&\text{(T1)} \quad \mathbf{H}(\mathbf{q}) = \mathbf{F}_0\ \widetilde{\mathbb{F}1}(\mathbf{q}) = \mathbf{F}_0\mathbf{J}_0\ \mathbf{A} = \mathbf{J}_0^{\text{curr}}\,\mathbf{A},\\
&\text{(T2)} \quad \mathbf{H}(\mathbf{q}) = \mathbf{F}_0\ \widetilde{\mathbb{F}2}(\mathbf{q}) = \mathbf{F}_0\mathbf{J}_0^{-T}\mathbf{A} = \mathbf{J}_0^{\text{curr}}\left(\mathbf{J}_0^{-1}\mathbf{J}_0^{-T}\right)\mathbf{A},\\
&\text{(T3)} \quad \mathbf{H}(\mathbf{q}) = \mathbf{F}_0^{-T}\ \widetilde{\mathbb{F}1}(\mathbf{q}) = \mathbf{F}_0^{-T}\mathbf{J}_0\ \mathbf{A} = (\mathbf{J}_0^{\text{curr}})^{-T}\left(\mathbf{J}_0^T\,\mathbf{J}_0\right)\mathbf{A},\\
&\text{(T4)} \quad \mathbf{H}(\mathbf{q}) = \mathbf{F}_0^{-T}\ \widetilde{\mathbb{F}2}(\mathbf{q}) = \mathbf{F}_0^{-T}\mathbf{J}_0^{-T}\mathbf{A} = (\mathbf{J}_0^{\text{curr}})^{-T}\,\mathbf{A},
\end{aligned} \tag{31}$$

where $\mathbf{A} \doteq \mathbf{G}(\mathbf{q})\ \mathbf{J}_0^{-1}\ (j_0/j)$ is the common part of all transformations. Note that the term $\left(\mathbf{J}_0^T\mathbf{J}_0\right)^{-1}$ of T2 does not appear in T4, so it can cause differences between the solutions for these transformations. Also the term $\left(\mathbf{J}_0^T\mathbf{J}_0\right)$ in T3 is not present in T1, which can have similar consequences.

Below we shortly address the selected properties of the above transformations.

1. *Objectivity under superposed rigid-body motion for T4* Let $\mathbf{x} = \boldsymbol{\varphi}(\mathbf{X})$ be the current position of a particle $\mathbf{X}$. Consider a motion superimposed on the current position $\mathbf{x}$, i.e. $\mathbf{x}^+ = \boldsymbol{\varphi}^+(\mathbf{x}) = \mathbf{Q}\mathbf{x} + \mathbf{c}$, where $\mathbf{Q} \in \mathrm{SO}(3)$ is the rotation tensor and $\mathbf{c}$ is the translation vector. Then the deformation gradient transforms as follows:

$$\mathbf{F}(\mathbf{x}^+) = \frac{\partial \mathbf{x}^+}{\partial \mathbf{X}} = \frac{\partial(\mathbf{Q}\mathbf{x}+\mathbf{c})}{\partial \mathbf{X}} = \mathbf{Q}\frac{\partial \mathbf{x}}{\partial \mathbf{X}} = \mathbf{Q}\,\mathbf{F}(\mathbf{x}). \tag{32}$$

For objectivity of the enhanced deformation gradient, $\mathbf{F}^{\text{enh}}(\mathbf{x},\mathbf{q})$, we require an analogous formula to be satisfied, i.e.

$$\mathbf{F}^{\text{enh}}(\mathbf{x}^+,\mathbf{q}) = \mathbf{Q}\,\mathbf{F}^{\text{enh}}(\mathbf{x},\mathbf{q}), \tag{33}$$

Using Eq. (20), rewritten as $\mathbf{F}^{\text{enh}}(\mathbf{x},\mathbf{q}) = \mathbf{F}(\mathbf{x}) + \mathbf{H}(\mathbf{x},\mathbf{q})$, we obtain

$$\mathbf{F}^{\text{enh}}(\mathbf{x}^+,\mathbf{q}) = \mathbf{Q}\,\mathbf{F}(\mathbf{x}) + \mathbf{Q}\,\mathbf{H}(\mathbf{x},\mathbf{q}). \tag{34}$$

Because the first term $\mathbf{Q}\,\mathbf{F}(\mathbf{x}) = \mathbf{F}(\mathbf{x}^+)$, hence the requirement of Eq. (33) reduces to

$$\mathbf{H}(\mathbf{x}^+,\mathbf{q}) = \mathbf{Q}\,\mathbf{H}(\mathbf{x},\mathbf{q}). \tag{35}$$

Considering the four transformations of Eq. (31), we note that they depend on the current position $\mathbf{x}$ through $\mathbf{F}_0$ as also $\mathbf{J}_0^{\text{curr}} = \mathbf{F}_0\mathbf{J}_0$ by Eq. (7). Hence we obtain

$$\begin{aligned}\mathbf{F}_0(\mathbf{x}^+) = \mathbf{F}(\mathbf{x}^+)\big|_0 &= \frac{\partial \mathbf{x}^+}{\partial \mathbf{X}}\bigg|_0 = \frac{\partial(\mathbf{Q}\mathbf{x}+\mathbf{c})}{\partial \mathbf{X}}\bigg|_0 = \mathbf{Q}\frac{\partial \mathbf{x}}{\partial \mathbf{X}}\bigg|_0\\ &= \mathbf{Q}\,\mathbf{F}(\mathbf{x})|_0 = \mathbf{Q}\,\mathbf{F}_0(\mathbf{x}),\end{aligned} \tag{36}$$

where "0" is the element's center. Using the definition of $\mathbf{H}$ of Eq. (31), the l.h.s. of Eq. (35) for T4 is

$$\mathbf{H}(\mathbf{x}^+,\mathbf{q}) = \mathbf{F}_0^{-T}(\mathbf{x}^+)\,\widetilde{\mathbb{F}2}(\mathbf{q}). \tag{37}$$

On the other hand, the r.h.s. of Eq. (35) for T4 is

$$\mathbf{Q}\,\mathbf{H}(\mathbf{x},\mathbf{q}) = \mathbf{Q}\,\mathbf{F}_0^{-T}\,\widetilde{\mathbb{F}2}(\mathbf{q}) = \mathbf{F}_0^{-T}(\mathbf{x}^+)\,\widetilde{\mathbb{F}2}(\mathbf{q}), \tag{38}$$

where $\mathbf{Q}\,\mathbf{F}_0(\mathbf{x}) = \mathbf{F}_0(\mathbf{x}^+)$ of Eq. (36) was used. The last form was obtained on use of $\mathbf{Q} = \mathbf{Q}^{-T}$, as then $\mathbf{Q}\,\mathbf{F}_0^{-T} = \mathbf{Q}^{-T}\,\mathbf{F}_0^{-T} = (\mathbf{Q}\,\mathbf{F}_0)^{-T} = \mathbf{F}_0^{-T}(\mathbf{x}^+)$. As both sides are equal, the requirement of Eq. (35) is satisfied and the enhancement $\mathbf{H}$ is objective for T4. The numerical test of objectivity is described in Sect. 5.2.2.

Remark The enhanced right Cauchy-Green deformation tensor $\mathbf{C}^{\text{enh}} \doteq (\mathbf{F}^{\text{enh}})^T\,\mathbf{F}^{\text{enh}}$ of arguments $(\mathbf{x}^+,\mathbf{q})$, on use of Eq. (33) becomes

$$\mathbf{C}^{\text{enh}} = (\mathbf{Q}\mathbf{F}^{\text{enh}})^T\,(\mathbf{Q}\mathbf{F}^{\text{enh}}) = (\mathbf{F}^{\text{enh}})^T\mathbf{Q}^T\mathbf{Q}\,\mathbf{F}^{\text{enh}} = (\mathbf{F}^{\text{enh}})^T\mathbf{F}^{\text{enh}}, \tag{39}$$

where $\mathbf{F}^{\text{enh}} = \mathbf{F}^{\text{enh}}(\mathbf{x},\mathbf{q})$, and $\mathbf{Q}^T\mathbf{Q} = \mathbf{I}$ was used. As $\mathbf{C}^{\text{enh}}$ is not affected by $\mathbf{Q}$, it is objective, but, obviously, it depends on the form of the enhancement.

2. *Rigid-body rotation* When $\mathbf{F}_0 = \mathbf{Q}_0$, where $\mathbf{Q}_0 \in \text{SO}(3)$, then both the transformations T2 and T4 become equal to $\mathbf{H}(\mathbf{q}) = \mathbf{Q}_0\,\widetilde{\mathbb{F}2}(\mathbf{q})$ on use of $\mathbf{F}_0^{-T} = \mathbf{Q}_0^{-T} = \mathbf{Q}_0$.

3. *Effect of transposition of* $\mathbf{G}$ *on linear strain* The enhanced linear strain is

$$\begin{aligned}\mathbf{E}^{\text{enh}} &= \mathbf{F}^{\text{enh}} + (\mathbf{F}^{\text{enh}})^T - 2\mathbf{I}\\ &= (\mathbf{F} + \mathbf{F}^T - 2\mathbf{I}) + \underline{(\mathbf{H} + \mathbf{H}^T)},\end{aligned} \tag{40}$$

where, for small deformations, the enhancement matrix $\mathbf{H} = \widetilde{\mathbb{F}1}(\mathbf{q})$ for T1 and T3, and $\mathbf{H} = \widetilde{\mathbb{F}2}(\mathbf{q})$ for T2 and T4. For the above defined four transformations, the underlined term becomes:

For T1 and T3,

$$(\mathbf{H} + \mathbf{H}^T) = \left[\mathbf{J}_0\;\mathbf{G}(\mathbf{q})\;\mathbf{J}_0^{-1} + \mathbf{J}_0^{-T}\;\mathbf{G}^T(\mathbf{q})\;\mathbf{J}_0^T\right]\frac{j_0}{j}, \tag{41}$$

For T2 and T4,

$$(\mathbf{H} + \mathbf{H}^T) = \mathbf{J}_0^{-T}\;\left[\mathbf{G}(\mathbf{q}) + \mathbf{G}^T(\mathbf{q})\right]\;\mathbf{J}_0^{-1}\frac{j_0}{j}. \tag{42}$$

We see that $(\mathbf{H} + \mathbf{H}^T)$ does not change under the transposition of $\mathbf{G}(\mathbf{q})$ for transformations T2 and T4, but it does for T1 and T3. In consequence, the linear solutions obtained using $\mathbf{G}^T(\mathbf{q})$ or $\mathbf{G}(\mathbf{q})$ are identical for T2 and T4, but are different for T1 and T3. Hence T1 and T3 are not suitable for the method of stabilization based on the transposition of $\mathbf{G}(\mathbf{q})$.

When comparing T2 to T4 for large deformations, their solutions are generally different, no matter whether $\mathbf{G}^T(\mathbf{q})$ or $\mathbf{G}(\mathbf{q})$ is used. The use of $\mathbf{G}^T(\mathbf{q})$ is beneficial, as it suppresses hourglassing at the critical strain for nearly-incompressible hyperelastic material, see Sect. 5.3.4.

4. *Variation of* $\mathbf{H}$ The variation of $\mathbf{H}(\mathbf{q})$ for the transformation rule T4 of Eq. $(31)_4$ is

$$\delta\mathbf{H}(\mathbf{q}) = \left[\delta(\mathbf{J}_0^{\text{curr}})^{-T}\;\mathbf{G}(\mathbf{q}) \;+\; (\mathbf{J}_0^{\text{curr}})^{-T}\;\delta\mathbf{G}(\mathbf{q})\right]\;\mathbf{J}_0^{-1}\;\frac{j_0}{j}. \tag{43}$$

The variation $\delta(\mathbf{J}_0^{\text{curr}})^{-1}$ is obtained by taking the variation of $(\mathbf{J}_0^{\text{curr}})^{-1}\mathbf{J}_0^{\text{curr}} = \mathbf{I}$, which yields

$$\delta(\mathbf{J}_0^{\text{curr}})^{-1} = -(\mathbf{J}_0^{\text{curr}})^{-1}\;\delta\mathbf{J}_0^{\text{curr}}\;(\mathbf{J}_0^{\text{curr}})^{-1}, \tag{44}$$

where $\delta\mathbf{J}_0^{\text{curr}}$ can be computed in a standard manner.

3.2 Representation EADG2 for enhancement H

The *0th order* part of the enhanced deformation gradient can be defined analogously to this part of strain in Eq. $(12)_1$. Using Eq. (20), we obtain

$$\mathbf{F}^{0\,\text{enh}}(\mathbf{u},\mathbf{q}) \;=\; \mathbf{F}^0(\mathbf{u}) + \underbrace{\mathbf{H}^0(\mathbf{u},\mathbf{G}(\mathbf{q},\boldsymbol{\xi}))}_{\text{EADG}}, \tag{45}$$

where $\mathbf{H}^0$ is the *0th order* enhancement matrix. For the transformation rule T4 of Eq. (31), we have

$$\mathbf{H}^0(\mathbf{u},\mathbf{G}(\mathbf{q})) = (\mathbf{J}_0^{\text{curr}})^{-T}\;\mathbf{G}(q_i,\;\xi,\eta)\;\mathbf{J}_0^{-1}\;\frac{j_0}{j}, \tag{46}$$

where $\mathbf{J}^{\text{curr}}$ is the current Jacobian matrix and $j \doteq \det\mathbf{J}$. The subscript "0" indicates the element's center. Analogous formulas for T1, T2 and T3 can be obtained from Eq. (31).

Using the idea explained in Eqs. (1) and (2), we employ a simple 2-parameter representation, designated EADG2, to define the matrix of representations

$$\mathbf{G}(q_i,\;\xi,\eta) \doteq \begin{bmatrix} 0 & q_1\eta_S & 0\\ q_2\xi_S & 0 & 0\\ 0 & 0 & 0\end{bmatrix}, \quad i = 1,2. \tag{47}$$

The skew coordinates ξ_S, η_S are defined as

$$\xi_S = \xi + A_{11}\,\xi\eta, \quad \eta_S = \eta + A_{21}\,\xi\eta, \tag{48}$$

where $A_{11} = (j_{,\eta})_0/j_0$, $A_{21} = (j_{,\xi})_0/j_0$ and $j = \det\mathbf{J}$. For parallelogram-shaped elements, $A_{11} = A_{21} = 0$, so the difference between the natural and skew coordinates vanishes, see [52, Sect. 3.2]. The so-defined $\mathbf{G}$ depends

on $\xi, \eta \in [-1, 1]$, but not on the thickness coordinate $\zeta \in [-1, 1]$.

Finally, we note that the *0th order* enhanced Green strain is defined as

$$2\mathbf{E}^{0\,\mathrm{enh}} = (\mathbf{F}^{0\,\mathrm{enh}})^T\ \mathbf{F}^{0\,\mathrm{enh}} - \mathbf{I}, \tag{49}$$

where $\mathbf{F}^{0\,\mathrm{enh}}$ is given by Eqs. (45–48).

4 New solid-shell elements free from hourglassing

In this section we describe three new solid-shell elements which are free from hourglassing. In all of these elements the transverse shear strain and thickness strain are treated as described in Sect. 2.1, while the *1st order* bending/twisting strain remains standard.

The *0th* and the *1st order* parts of the stress, strain and deformation gradient w.r.t. the thickness coordinate ζ are designated respectively by the superscript "0" and "1".

4.1 HW element with EADG enhancement

In this section we use the Hu–Washizu solid-shell element HW19 of [52] as the parent element, and describe its modifications to create the new element HW18/EADG2, which is free from mesh hourglassing.

4.1.1 Parent element HW19

The 8-node solid-shell element HW19 is based on the *partial/enhanced* Hu–Washizu functional,

$$\begin{aligned}\widetilde{F}_{\mathrm{HW19}} \doteq \int_B \Big\{ & \mathcal{W}(E^{0\,*}_{\alpha\beta} + \zeta E^{1}_{\alpha\beta} + \zeta E^{1\,\mathrm{EAS}}_{\alpha\beta}, E^{0\,\mathrm{ANS}}_{33} \\ & + \zeta E^{1\,\mathrm{EAS}}_{33}, E^{0\,\mathrm{ANS}}_{\alpha 3}) \\ & + \underline{S^{0\,*}_{\alpha\beta} \cdot [E^{0}_{\alpha\beta} - E^{0\,*}_{\alpha\beta}]} \Big\}\, dV - \ F_{ext},\end{aligned} \tag{50}$$

where $\mathcal{W}$ is the strain energy density, F_{ext} is the potential of the external loads and the body force, and V is the volume of the 3D body in the initial configuration B.

The Lagrange multiplier method is applied only to the in-plane strain components, see the underlined term, where $S^{0\,*}_{\alpha\beta}$ is the assumed Lagrange multiplier, $E^{0\,*}_{\alpha\beta}$ is the assumed strain and $E^{0}_{\alpha\beta}$ is the compatible strain. Note that $\zeta E^{1\,\mathrm{EAS}}_{\alpha\beta}$ and $\zeta E^{1\,\mathrm{EAS}}_{33}$ result from the enhancement of thickness strain of Eq. (17), while the terms $E^{0\,\mathrm{ANS}}_{33}$ and $E^{0\,\mathrm{ANS}}_{\alpha 3}$ from the ANS method of Eq. (15), see Sect. 2.1.

Assumed stress/strain representations In the element HW19, all the assumed stress/strain representations are ζ -independent, and are defined as follows:

1. The assumed CTV stress representation is defined as

$$\begin{aligned}\mathbf{A}_{\mathrm{v}} &= [q_1, q_2, 0,\ q_3, 0, 0]^T, \\ \mathbf{C}_{\mathrm{v}} &\doteq [C_{11}, C_{22}, 0,\ 0, 0, 0]^T,\end{aligned} \tag{51}$$

   where $C_{11} = q_4\, \eta_S$ and $C_{22} = q_5\, \xi_S$. This is the 5-parameter stress representation of Pian and Sumihara [34] but expressed in skew coordinates ξ_S, η_S defined in Eq. (48). The CTV $\rightarrow$ CART transformation of components of stress is

$$\mathbf{S}^{a}_{\mathrm{v}} = \mathbf{T}^{0}_{\mathrm{S}}\, \mathbf{A}_{\mathrm{v}} + \mathbf{T}^{\zeta=0}_{\mathrm{S}}\, \mathbf{C}_{\mathrm{v}}, \tag{52}$$

   where $\mathbf{T}^{0}_{\mathrm{S}}$ is computed at the element's center (superscript "0") and at the reference surface (superscript "$\zeta = 0$"). Components $S^{0\,*}_{\alpha\beta}$ are extracted from the vector $\mathbf{S}^{a}_{\mathrm{v}}$.

2. The assumed CTV strain representation is defined as follows:

$$\begin{aligned}\mathbf{A}_{\mathrm{v}} &= [q_1, q_2, 0,\ q_3, 0, 0]^T, \\ \mathbf{C}_{\mathrm{v}} &\doteq [C_{11}, C_{22}, 0,\ C_{12}, 0, 0]^T,\end{aligned} \tag{53}$$

   where $C_{11} = q_4\, \xi_S + q_5\, \eta_S + \underline{q_6\, \xi_S \eta_S}$, $C_{22} = q_7\, \xi_S + q_8\, \eta_S + \underline{q_9\, \xi_S \eta_S}$ and $C_{12} = q_{10}\, \xi_S + q_{11}\, \eta_S$. In total 11 parameters. The CTV $\rightarrow$ CART transformation of components of strain is

$$\mathbf{E}^{a}_{\mathrm{v}} = \mathbf{T}^{0}_{\mathrm{E}}\, \mathbf{A}_{\mathrm{v}}\ +\ \mathbf{T}^{\zeta=0}_{\mathrm{E}}\, \mathbf{C}_{\mathrm{v}}, \tag{54}$$

   where $\mathbf{T}^{0}_{\mathrm{E}}$ is computed at the element's center (superscript "0") and at the reference surface (superscript "$\zeta = 0$"). Components $E^{0\,*}_{\alpha\beta}$ are extracted from the vector $\mathbf{E}^{a}_{\mathrm{v}}$. The CTV $\rightarrow$ CART transformation is used for the assumed strains because then the results are more accurate than for the COV $\rightarrow$ CART transformation, when the reduced representations are assumed, see [53].

The above transformation operators $\mathbf{T}_{\mathrm{S}}$ and $\mathbf{T}_{\mathrm{E}}$ as well as the stress/strain vectors are defined in Appendix 1. In total, the element HW19 involves 19 additional parameters q_i: 5 for the assumed stress, 11 for the assumed strain and 3 to enhance the thickness strain.

Remark If the underlined terms of C_{11} and C_{22} in Eq. (53) are omitted then for the nearly-incompressible material, 2 large eigenvalues appear. The eigenvector associated with the second large eigenvalue is shown in Fig. 3.

It is the scaled vector of nodal vertical displacements $[-1,1,-1,1,\ 1,-1,1,-1]$, for which the element's volume remains unchanged. It resembles the h_{4I} mode for the 8-node solid 3D element of [4, Fig. 4]. The underlined terms in C_{11} and C_{22} eliminate the second large eigenvalue and this eigenvector.

4.1.2 New element HW18/EADG2

This element is obtained from the parent element HW19 by adding the 2-parameter EADG enhancement to the in-plane compatible strain $E^0_{\alpha\beta}$ in the Lagrange multiplier term. The governing *partial/enhanced* Hu–Washizu functional is as follows:

$$\begin{aligned}\widetilde{F}_{\mathrm{HW18/EADG2}} \doteq \int_B \{\mathcal{W}(E^{0\,*}_{\alpha\beta} + \zeta E^1_{\alpha\beta} + \zeta E^{1\,\mathrm{EAS}}_{\alpha\beta}, E^{0\,\mathrm{ANS}}_{33} \\ + \zeta E^{1\,\mathrm{EAS}}_{33}, E^{0\,\mathrm{ANS}}_{\alpha 3}) \\ + S^{0\,*}_{\alpha\beta} \cdot \left[\underline{E^{0\,\mathrm{enh}}_{\alpha\beta}} - E^{0\,*}_{\alpha\beta}\right]\} \ dV - \ F_{ext}.\end{aligned} \tag{55}$$

Two important changes have been introduced into $\widetilde{F}_{\mathrm{HW19}}$ of Eq. (50) to obtain the above functional:

1. The *0th order* enhanced strain $E^{0\,\mathrm{enh}}_{\alpha\beta}$ (underlined in Eq. (55)) has replaced the standard $E^0_{\alpha\beta}$, which is used in Eq. (50). $E^{0\,\mathrm{enh}}_{\alpha\beta}$ is obtained using the EADG enhancement of the deformation gradient described in Sect. 3.2, see Eqs. (45–48). It uses the transformation rule T4 and the 2-parameter EADG2 representation.
2. The assumed representation of stress $S^{0\,*}_{\alpha\beta}$ is modified by adding the non-zero component $C_{12} = q_6\,\xi_S + q_7\,\eta_S$. Then the assumed CTV stress representation is defined by two vectors:

$$\begin{aligned}\mathbf{A}_{\mathrm{v}} &= [q_1, q_2, 0,\ q_3, 0, 0]^T, \\ \mathbf{C}_{\mathrm{v}} &\doteq [C_{11}, C_{22}, 0,\ C_{12}, 0, 0]^T,\end{aligned} \tag{56}$$

where C_{11} and C_{22} remain unmodified. Hence, in total, 7 parameters q_i are used for the assumed stress, and the CTV $\rightarrow$ CART transformation of the stress components of Eq. (52).

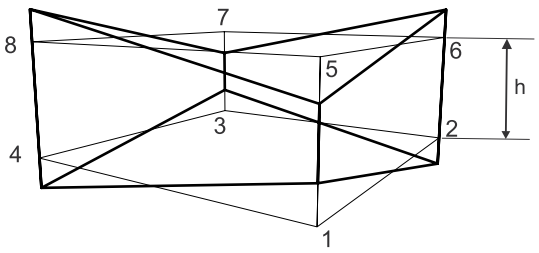

Fig. 3 Eigenvector associated with the second large eigenvalue (thick line) superimposed on the solid-shell element (thin line)

The assumed strain $E^{0\,*}_{\alpha\beta}$ is unmodified, compared to the element HW19. The remaining terms in $\widetilde{F}_{\mathrm{HW18/EADG2}}$ are treated identically as in $\widetilde{F}_{\mathrm{HW19}}$.

In total, the element HW18/EADG2 involves 23 additional parameters q_i: 7 for the assumed stress, 11 for the assumed strain, 3 for the EAS3 representation of the *1st order* enhanced thickness strain and 2 for the EADG2 enhancement to prevent hourglassing.

4.2 EAS element with EADG enhancement

In this section we use the solid-shell element EAS10 as the parent element, and modify it to obtain the new element EAS5/EADG2, which is free from mesh hourglassing.

4.2.1 Parent element EAS10

The 8-node solid-shell element EAS10 is based on the *Enhanced Assumed Strain* (EAS) method of Simo and Rifai [41], and involves 10 parameters. The first version of this element in Klinkel et al. [22] used one parameter in the EAS enhancement of the *1st order* thickness strain. Two additional parameters were added in Vu-Quoc and Tan [44] to pass the out-of-plane bending patch test.

The EAS10 element is based on the *enhanced* potential energy functional,

$$\begin{aligned}F^{\mathrm{enh}}_{\mathrm{PE}}(\mathbf{u},\mathbf{q}) \doteq \int_B \mathcal{W}\Big((\mathbf{E}^0(\mathbf{u}) + \mathbf{E}^{0\,\mathrm{EAS}}(\mathbf{u},\mathbf{q})) \\ + \zeta\ (\mathbf{E}^1(\mathbf{u})\ +\ \mathbf{E}^{1\,\mathrm{EAS}}(\mathbf{u},\mathbf{q}))\Big)\, dV - \ F_{ext},\end{aligned} \tag{57}$$

where $\mathcal{W}$ is the strain energy density. The *0th order* enhanced strain consists of two components

$$\begin{aligned}\mathbf{E}^0(\mathbf{u}) &= \mathbf{J}^{-T}_{\zeta=0}\ \mathbf{E}^{0\ \mathrm{COV}}(\mathbf{u})\ \mathbf{J}^{-1}_{\zeta=0}, \\ \mathbf{E}^{0\ \mathrm{EAS}}(\mathbf{u},\mathbf{q}) &= \mathbf{J}^{-T}_0\ \mathbf{G}(\mathbf{q})\ \mathbf{J}^{-1}_0\ \frac{j_0}{j},\end{aligned} \tag{58}$$

where $\mathbf{E}^0(\mathbf{u})$ is the compatible strain computed as outlined in Eq. $(10)_2$ and $\mathbf{E}^{0\ \mathrm{COV}}$ is the matrix of covariant components. The second component $\mathbf{E}^{0\ \mathrm{EAS}}(\mathbf{u},\mathbf{q})$ is the EAS enhancement of the in-plane strains, which includes the following 7-parameter (symmetric) representation EAS7,

$$\begin{aligned}\mathbf{G}(q_i,\ \xi,\eta) \doteq \begin{bmatrix} q_1\xi + q_2\,\xi\eta & q_5\xi + q_6\eta + q_7\,\xi\eta & 0 \\ \mathrm{sym.} & q_3\eta + q_4\,\xi\eta & 0 \\ 0 & 0 & 0 \end{bmatrix}, \\ i = 1,\ldots,7.\end{aligned} \tag{59}$$

The transformations used in Eq. (58) are obtained from Eq. $(9)_2$ and $\mathbf{J}^{-1}$ is computed at the reference surface (subscript "$\zeta = 0$") and at the element's center (subscript "0").

The *1st order* compatible strain $\mathbf{E}^1(\mathbf{u})$ is defined in Eq. (12)$_2$, while $\mathbf{E}^{1\,\mathrm{EAS}}(\mathbf{u},\mathbf{q})$ is the enhancement of thickness strain, and is computed as outlined in Eq. (18).

The EAS10 element suffers from the mesh hourglassing at the critical strain for nearly-incompressible materials, see the test of Sect. 5.3.4.

4.2.2 New element EAS5/EADG2

This element is obtained from the parent element EAS10 by implementing two modifications of the *0th order* strains: (1) the 2-parameter EADG enhancement is added to eliminate hourglassing, and (2) the EAS7 representation is reduced to the EAS5 representation. The resulting element EAS5/EADG2 is free from mesh hourglassing.

The 8-node solid-shell element EAS5/EADG2 is based on the *enhanced* potential energy functional,

$$\begin{aligned} &F^{\mathrm{enh}}_{\mathrm{EAS5/EADG2}}(\mathbf{u},\mathbf{q}) \\ &\doteq \int_B \mathcal{W}\Big((\mathbf{E}^0(\mathbf{u}) + \mathbf{E}^{0\,\mathrm{EAS}}(\mathbf{u},\mathbf{q}) \\ &\quad + \underline{\mathbf{E}^{0\,\mathrm{enh}}(\mathbf{F}^{0\,\mathrm{enh}}(\mathbf{u},\mathbf{q}))}) + \zeta(\mathbf{E}^1(\mathbf{u}) + \mathbf{E}^{1\,\mathrm{EAS}}(\mathbf{u},\mathbf{q})) \Big) \\ &\quad dV - F_{ext}, \end{aligned} \tag{60}$$

where the underlined term is added. Regarding the *0th order* terms, $\mathbf{E}^{0\,\mathrm{enh}}(\mathbf{F}^{0\,\mathrm{enh}}(\mathbf{u},\mathbf{q}))$ is defined in Eq. (49) using the enhanced deformation gradient $\mathbf{F}^{0\,\mathrm{enh}}$ with the transformation rule T4 and the EADG2 representation, see Eqs. (45–48). Besides, $\mathbf{E}^{0\,\mathrm{EAS}}(\mathbf{u},\mathbf{q})$ is defined as for the parent element EAS10, i.e. using Eq. (58), but with the EAS5 representation defined below.

EAS5 representation Due to the presence of $q_1\eta_S$ and $q_2\xi_S$ in the EADG2 representation of Eq. (47), the terms ξq_5 and ηq_6 must be omitted in the EAS7 representation of Eq. (59). This yields the (symmetric) EAS5 representation,

$$\mathbf{G}(q_i,\ \xi,\eta) \doteq \begin{bmatrix} q_1\xi + q_2\,\xi\eta & q_5\,\xi\eta & 0 \\ & q_3\eta + q_4\,\xi\eta & 0 \\ \mathrm{sym.} & & 0 \end{bmatrix}, \quad i = 1,\ldots,5. \tag{61}$$

The *1st order* terms, i.e. the compatible strain $\mathbf{E}^1(\mathbf{u})$ and the enhancement of the thickness strain $\mathbf{E}^{1\,\mathrm{EAS}}(\mathbf{u},\mathbf{q})$ are treated as in the element EAS10.

In total the element EAS5/EADG2 involves 10 additional parameters q_i: 5 for the EAS5 representation and 2 for the EADG2 representation, both in the enhancements to the *0th order* membrane strain, and 3 for the EAS3 representation of the *1st order* enhanced thickness strain.

4.3 New EADG7 element

In this section the solid-shell element with the *0th order* in-plane part enhanced by the EADG method is described. The standard EADG4 representation is sufficient to suppress the mesh hourglassing by transposition of $\mathbf{G}$ but additional 3 parameters are added to eliminate one of the two large eigenvalues for the nearly incompressible hyperelastic material and to improve the bending behavior.

The 8-node solid-shell element EADG7 is based on the *enhanced* potential energy functional,

$$\begin{aligned} &F^{\mathrm{enh}}_{\mathrm{EADG7}}(\mathbf{u},\mathbf{q}) \\ &\doteq \int_B \mathcal{W}\left((\mathbf{E}^0(\mathbf{u}) + \mathbf{E}^{0\,\mathrm{enh}}(\mathbf{F}^{0\,\mathrm{enh}}(\mathbf{u},\mathbf{q})) \right. \\ &\quad \left. + \zeta\ (\mathbf{E}^1(\mathbf{u}) + \mathbf{E}^{1\,\mathrm{EAS}}(\mathbf{u},\mathbf{q})) \right) dV - F_{ext}, \end{aligned} \tag{62}$$

where $\mathcal{W}$ is the strain energy density. Note that *0th order* term $\mathbf{E}^{0\,\mathrm{enh}}(\mathbf{F}^{0\,\mathrm{enh}}(\mathbf{u},\mathbf{q}))$ is defined in Eq. (49) using the enhanced deformation gradient $\mathbf{F}^{0\,\mathrm{enh}}$ with the transformation rule T4 and the EADG7 representation, which is defined below.

The *1st order* compatible strain $\mathbf{E}^1(\mathbf{u})$ is defined as in Eq. (12)$_2$, while $\mathbf{E}^{1\,\mathrm{EAS}}(\mathbf{u},\mathbf{q})$ is the enhancement of the thickness strain, which is computed as in Eqs. (18) and (19).

EADG7 representation of the enhancement of deformation gradient Recall that the standard 4-parameter representation EADG4 is

$$\mathbf{G}(q_i,\ \xi,\eta) \doteq \begin{bmatrix} q_1\xi & q_3\eta & 0 \\ q_4\xi & q_2\eta & 0 \\ 0 & 0 & 0 \end{bmatrix}, \quad i = 1,\ldots,4. \tag{63}$$

and it does suppress the mesh hourglassing when transposed. However, the solid-shell element based on the EADG4 yields two very large eigenvalues instead of one, in the eigenvalue test for nearly incompressible hyperelastic material ($\nu = 0.499999999$), see Sect. 5.1. As a remedy, the following 7-parameter representation EADG7 is proposed,

$$\mathbf{G}(q_i,\ \xi,\eta) \doteq \begin{bmatrix} q_1\xi + \underline{q_5\,\xi\eta} & q_3\eta + \underline{q_6\,\xi\eta} & 0 \\ q_4\xi & q_2\eta + \underline{q_7\,\xi\eta} & 0 \\ 0 & 0 & 0 \end{bmatrix}, \quad i = 1,\ldots,7, \tag{64}$$

where three bi-linear (underlined) terms are added to the EADG4 representation. The diagonal terms with q_5 and q_7 remove one large eigenvalue for nearly incompressible hyperelastic material. The off-diagonal term with q_6 improves the bending behavior, see the "Twisted beam" test of Sect. 5.3.3.

In total, the element EADG7 involves 10 additional parameters $q_i : 7$ for the EADG7 enhancement of the *0th order* membrane strain and 3 for the EAS3 enhancement of the *1st order* thickness strain.

Remark Note that both, the *1st order* thickness strain E_{33}^1 of Eq. (18) and the EADG enhancement for the transformation T4 of Eq. (46), utilize the "COV → CART" transformation, the latter through $\widetilde{\mathbb{F}2}(\mathbf{q})$. Hence, the EADG method and transformation T4 can be tested as a replacement for the EAS method for the thickness strain E_{33}^1. Then in the *enhanced* potential energy functional of Eq. (62), $\mathbf{E}^{1\,\mathrm{EAS}}(\mathbf{u},\mathbf{q})$ is replaced by

$$\mathbf{E}^{1\,\mathrm{enh}}(\mathbf{u},\mathbf{q}) = (\mathbf{J}_0^{\mathrm{curr}})^{-T}\ \mathbf{G}^1(\mathbf{q})\ \mathbf{J}_0^{-1}\ \frac{j_0}{j}, \tag{65}$$

where $\mathbf{G}^1(\mathbf{q})$ is given by Eq. (19). In the tests of Sect. 5, the modified element yielded the solutions which are similar to those for the element EADG7, but not always identical.

2D check of EADG7 representation Let us consider for simplicity a bi-unit (2×2) square element, for which the initial position vector components are $X_1 = \xi$ and $X_2 = \eta$. Then $\mathbf{J}$ is the identity matrix and the EADG enhancement of Eq. (46) is reduced to $\mathbf{H}^0(\mathbf{q}) = \mathbf{G}(q_i,\ \xi,\eta)$. Only the upper 2×2 sub-matrices of $\mathbf{H}^0(\mathbf{q})$ and $\mathbf{G}$ are considered below. For bi-linear shape functions, the compatible displacements are

$$u(\xi,\eta) = u_0 + \xi\, u_1 + \eta\, u_2 + \xi\eta\, u_3,$$
$$v(\xi,\eta) = v_0 + \xi\, v_1 + \eta\, v_2 + \xi\eta\, v_3,$$

where u_i and v_i $(i = 0,1,2,3)$ are functions of the nodal displacements. Then the deformation gradient and the enhancement using the EADG7 representation of Eq. (64) are

$$\mathbf{F}^0 = \begin{bmatrix} 1+u_1+\eta\, u_3 & u_2+\xi\, u_3 \\ v_1+\eta\, v_3 & 1+v_2+\xi\, v_3 \end{bmatrix},$$
$$\mathbf{H}^0 = \begin{bmatrix} q_1\xi + q_2\,\xi\eta & q_5\eta + q_6\,\xi\eta \\ q_7\xi & q_3\eta + q_4\,\xi\eta \end{bmatrix},$$

and the enhanced deformation gradient is $\mathbf{F}^{0\,\mathrm{enh}} = \mathbf{F}^0 + \mathbf{H}^0$. The enhancement $\mathbf{H}^0$ cannot be arbitrary; the restrictions are discussed in Simo and Armero [39] and Simo et al. [40, see (i) and (ii) on p. 365 and Eq. (3.3)]. For the above $\mathbf{F}^{0\,\mathrm{enh}}$, we can check that: (i) The components of $\mathbf{H}^0$ are not present in $\mathbf{F}^0$, when considered component by component. This precludes the rank deficiency of the tangent matrix and ensures stability of the method. (ii) The integral of a variation of the enhancement matrix $\mathbf{H}^0$ over the element's domain must vanish, $\int_V \delta\mathbf{H}^0\ dV = \mathbf{0}$. This condition results from the L_2 -orthogonality of $\delta\mathbf{H}^0$ to the (assumed) constant stress field and is a counterpart of the patch test. For the EADG7 representation, we obtain

$$\begin{bmatrix} \delta q_1\,\xi + \delta q_2\,\xi\eta & \delta q_5\,\eta + \delta q_6\,\xi\eta \\ \delta q_7\,\xi & \delta q_3\,\eta + \delta q_4\,\xi\eta \end{bmatrix} d\eta\, d\xi = \begin{bmatrix} 0 & 0 \\ 0 & 0 \end{bmatrix}. \tag{66}$$

On use of $\mathbf{F}^{0\,\mathrm{enh}}$, the enhanced linear strain is

$$\mathbf{E}^{0\,\mathrm{enh}} = \begin{bmatrix} u_1+\eta\, u_3 & \frac{1}{2}[(u_2+v_1)+\xi\, u_3+\eta\, v_3] \\ \mathrm{sym.} & v_2+\xi\, v_3 \end{bmatrix} + \begin{bmatrix} q_1\xi + \underline{q_2\,\xi\eta} & \frac{1}{2}[q_7\xi + q_5\eta + \underline{q_6\,\xi\eta}] \\ \mathrm{sym.} & q_3\eta + \underline{q_4\,\xi\eta} \end{bmatrix},$$

and after summing up these two matrices, all components are bi-linear polynomials. For the standard EADG4 representation, the bi-linear (underlined) terms are omitted.

5 Numerical tests

This section describes numerical tests of the three new 8-node solid-shell elements proposed in the current paper, see Table 2. In all of the elements the mesh hourglassing at the critical point is effectively suppressed by transposition of the representation matrix $\mathbf{G}$ in the EADG enhancement $\mathbf{H}$. The EADG enhancement is characterized by a pair of features (transformation rule, original/transposed form of $\mathbf{G}$), see Sect. 3. The EADG (T4,$\mathbf{G}^T$) enhancement is of particular interest.

These elements are based on the Green strain and developed from either the *partial/enhanced* Hu–Washizu functional (HW18/EADG2) or the *enhanced* potential energy functional (EAS5/ EADG2 and EADG7). The element' name characterizes only its in-plane part, which is a convention different to that used in [52].

All new solid-shell elements are identical in the following aspects: (a) the 3-parameter EAS enhancement to the *1st-order* thickness strain E_{33}^1 is applied, (b) the ANS methods are applied to the *0th order* strains: the transverse shear strains $E_{\alpha 3}^0$ and the thickness strain E_{33}^0, and (c) the *1st order* bending/twisting part remains standard (unmodified), (d) the $2\times 2\times 2$ Gauss rule is used to integrate the elements.

The last column in Table 2 shows the total number of additional elemental parameters q_i. They are eliminated at the element's level and updated by the scheme U2, see [48].

The *0th* and *1st order* parts of stress/strain (w.r.t. the thickness coordinate ζ) are respectively designated by the superscripts "0" and "1". In the sequel, "parameter" is abbreviated to "p".

Three solid-shell elements are used for reference:

Table 2 Characteristics of the tested/reference solid-shell 8-node elements

Element	Enhancement of membrane part	Assumed membrane stress/strain	Total number of parameters
Tested new solid-shell			
HW18/EADG2	EADG 2p, Eq. (47)	7p/11p, Eqs. (56/53)	23p
EAS5/EADG2	EAS 5p, Eq. (61) and EADG 2p, Eq. (47)	–	10p
EADG7	EADG 7p, Eq. (64)	–	10p
Ref. solid-shell			
HW19* [52]	–	5p/11p, Eqs. (51/53)	19p
EAS10*	EAS 7p, Eq. 59)	–	10p
HSEE* [23]	EAS 4p	18p/18p	43p

( )* our implementation

1. The element HW19 is based on the *partial/enhanced* Hu–Washizu functional, in which the Lagrange multiplier method is applied only to the membrane strain components. It includes the 3-parameter EAS enhancement of the *1st order* thickness strain of Eq. (17), but does not use the EADG enhancement.
2. The element EAS10 uses the 7-parameter EAS enhancement of the in-plane strains of Wilson et al. [47],

$$\widetilde{E}_{11}^{\mathrm{COV}} = q_1\xi + q_2\xi\eta, \quad \widetilde{E}_{22}^{\mathrm{COV}} = q_3\eta + q_4\xi\eta, \\ \widetilde{E}_{12}^{\mathrm{COV}} = q_5\xi + q_6\eta + q_7\xi\eta, \tag{67}$$

   and the 3-parameter EAS enhancement of the *1st order* thickness strain of Eq. (17). The initial version of this element of [22] used only q_1 in $\mathrm{G}_{33}^{1\,\mathrm{COV}}$ in Eq. (17). The linear terms $q_2\xi$ and $q_3\eta$ were added later to pass the bending patch test in [44]. In total, this element involves 10p, and does not use the EADG enhancement.

3. The HSEE element with 43 parameters of Klinkel et al. [23] is a Hu–Washizu type element; it is also described and compared to our HW35 element in [52, Sect. 3.4.2].

All these elements show mesh hourglassing at the critical point for the incompressible hyperelastic material. Also several other elements are used for comparison, including a 3D solid element and the Reissner-Mindlin shell elements with 6 dofs/node.

Modifications of 3D TSCG12 element for shell applications The 3D solid element TSCG12 is the 8-node hexahedron of Korelc et al. [24], and we use it for reference. To improve its accuracy in shell applications, we have introduced the following modifications:

1. The local (elemental) reference basis is constructed in the same way as for solid-shell elements, see Sect. 2, and transformations of the tangent stiffness matrix and the residual vector between the local and the global reference bases are performed. Note that for 3D elements the local basis is usually constructed differently. When the global reference basis is used for the TSCG12 element, the inward and outward displacements at the forces applied to the pinched hemisphere of Sect. 5.3.2 are not equal, even though they should be so in a linear test. This is caused by the reduced matrices $\mathbf{H}_{\mathrm{u}}$ and $\mathbf{H}_{\mathrm{b}}^{\mathrm{T}}$ which are used in the original TSCG12 element, and this issue is partly alleviated by using a local (elemental) reference basis.
2. The $2 \times 2 \times 2$-point Gauss integration is used as being more suitable for bending of elastic shells than the special 9-point rule, which serves as a replacement of the $3 \times 3 \times 3$-point Gauss integration in [40], and is rather intended for plasticity, which remains beyond the scope of the current paper.

In effect, the solutions yielded by the modified element 3D TSCG12 are closer to the solid-shell solutions than those yielded by the original element.

All our elements are derived using the symbolic system for automatic code generation, code optimization and automatic differentiation AceGen developed by J. Korelc [26] and are tested within the finite element program FEAP developed by R. L. Taylor [43, 57]. We gratefully acknowledge the use of these programs. Our parallel multithreaded (OMP) version of FEAP is described in [21].

We tacitly assume that any consistent set of units is used for the data defined in numerical examples.

5.1 Eigenvalues of a single element

The eigenvalues of the tangent matrix are computed for a single unsupported element, and for the Young's modulus $E = 1$ and the Poisson's ratio $\nu = 0.3$. Several element's shapes described in our recent paper [52, Sect. 5.1] are tested, and for all of them, the new solid-shell elements have the correct number of zero eigenvalues (6).

For all new solid-shell elements, one large eigenvalue and 6 zero eigenvalues is obtained for $\nu = 0.499999999$ and the truncated pyramid shape of Fig. 4. This shape is obtained from a hexahedron of size $2 \times 2 \times 0.1$ by shifting

its nodes by the vectors $[\pm 0.1, \pm 0.1, 0]$. We note that for the element EADG7, one of two large eigenvalues is eliminated due to 2 additional modes added to the diagonal of $\mathbf{G}$, see Sect. 4.3.

5.2 Linear tests

5.2.1 Patch tests

The shell-type patch tests (membrane and bending) are adapted and performed as described in [52, Sect. 5.2.1]. The tested solid-shell elements yield the correct displacements at the internal nodes and compatible strains at Gauss Points.

The standard 3D patch test is failed by the solid-shell elements, which is caused by the ANS method for the transverse shear strains. (The ANS method for the *1st order* thickness strain has no such consequence.) In contrast, the 3D 8-node hexahedron solid elements fail the shell-type bending patch test. Hence, for the bending dominated shell-type applications, the solid-shell elements are preferable to the 3D elements.

5.2.2 Objectivity test

This test was proposed to check objectivity of the enhanced 4-node 2D plane strain elements and the Ogden's material in Glaser and Armero [12, Example 4.3]. We adapt it here for the solid-shell elements and use the hyperelastic material.

The beam is strained and rotated in the X0Z plane, see Fig. 5a. Both ends of the beam are clamped. Strains are generated by the transversal shift of the right end by $d = 2\,h$, where h is the beam's height. Next the strained beam is rigidly rotated up to $90°$, which is controlled by the displacements applied to boundary nodes at the left and right ends. The boundary conditions are specified as in [12, Eqs. (30) and (31)], and the Newton method is used to solve the equilibrium equations.

The data is as follows: the beam length $L = 1.0$, height $h = 0.1$. The size in the 0Y direction $b = 1.0$, and to enable comparison with the plane strain results the 0Y-displacements are constrained. The neo-Hookean hyperelastic material of Eq. (68) with $\mu = 100$, the bulk modulus $K = 116.666666(6)$ and $\beta = -2$ is used. These values of μ and K correspond to the material constants, which are used in [12] for the Ogden's material.

For each rotation increment, the beam-type axial force N and transverse shear force Q, and the bending moment M are calculated using the reaction forces at the left end nodes. For the solid-shell element EADG7 with the enhancement (T4,$\mathbf{G}^T$) the beam-type forces and moment are shown in Fig. 5b. Two orientations of the solid-shell element are tested, with the nodal "directors" parallel to either the 0Z-axis or the 0Y-axis, which we designate "dir 0Z" and "dir 0Y", respectively. We see in this figure that the lines for both orientations of this element coincide. Similar solutions are obtained also for the other tested solid-shell elements.

The 2D reference results obtained using two 4-node plane strain elements are designated as follows: (a) "2D EADG4"—our EADG4 element and the hyperelastic material of Eq. (68), (b) "feap enha"—the enhanced element of FEAP [43] and the hyperelastic material, and (c) "2D Q1/ET4 Ogden"—the Q1/ET4 element and the Ogden's material taken from Glaser and Armero [12, Fig. 13].

In conclusion, the obtained N, Q and M are constant w.r.t. the rotation angle, which means that the strained enhanced solid-shell elements are invariant to the rigid-body rotation. Hence, the transformation used in the enhancement (T4,$\mathbf{G}^T$) is correct.

5.2.3 Two-element distortion test

The cantilever is modeled by two solid-shell elements, and a tilt of their common side is defined by the parameter d, see Fig. 6. The data is as follows: $E = 1500$, $\nu = 0$, $h = 1$, and $P = 10$. The nodes shown in Fig. 6 are doubled to create a mesh for the 8-node solid-shell elements. The pair of forces $\pm P$ is replaced by four forces $\pm P/2$. The applied boundary conditions are as described in [23].

This test is used to separately verify the in-plane part and the through-thickness part of solid-shell elements. Bending takes place in the X0Y plane, and two orientations of the elements are tested, i.e. the nodal "directors" are either parallel to the 0Z-axis (in-plane bending) or belong to the X0Y-plane (out-of-plane bending). Displacement u_y at the tip for a changing d is shown in Figs. 7 and 8. The EADG enhancement used with (T4,**G{}^T**) and (T4,**G**) gave identical results. The reference solutions are indicated by broken lines.

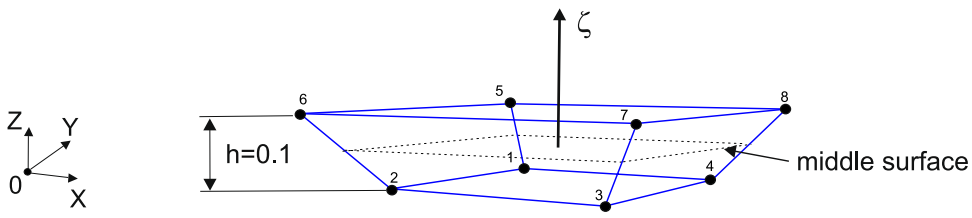

Fig. 4 Truncated pyramid (not to scale)

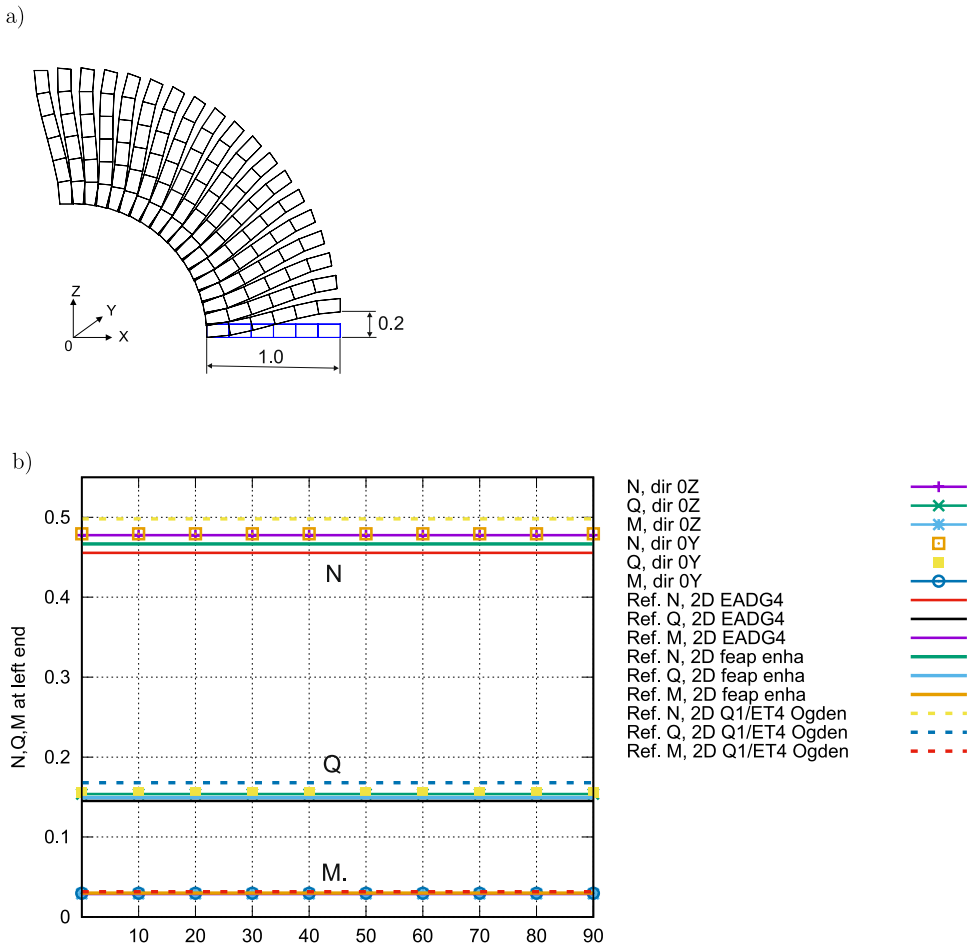

Fig. 5 Objectivity. **a** Scheme of the test, **b** N, Q and M for two orientations of the solid-shell element EADG7 (T4,$\mathbf{G}^T$) and the hyperelastic material

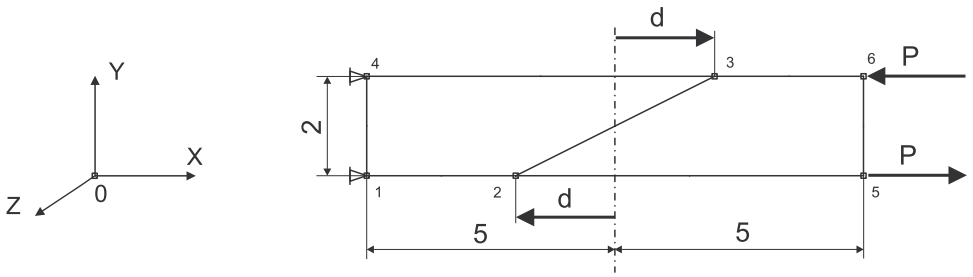

Fig. 6 Two-element distortion test. Initial geometry and load

1. The solutions for the in-plane bending are shown in Fig. 7. For $d \leq 2$, the most accurate is the tested element HW18/EADG2, next the reference HSEE and then the tested EAS5/EADG2 and EADG7, and the reference EAS10. The latter three elements yield identical results. When $d > 2$, i.e. beyond the range of practical use, most of the curves ascend for increasing d, and the smaller the ascension the better in this range. Refer to the discussion of this issue in [52, Sec. 5.2.4].
2. The solutions for the out-of-plane bending are shown in Fig. 8. All the tested elements yield an analytical solution $u_y = 1$ in the whole range of d. The reference solid-shells HW19 and EAS10 of [52] have similar accuracy. For the reference solid-shell HSEE, the error grows with the distortion d, which is also characteristic for the HW51 element of [52].

5.2.4 Straight cantilever of trapezoidal elements

This classical 2D test by MacNeal and Harder [28] can also be applied to transverse deformation of solid-shell elements, as in Harnau et al. [18]. The accuracy of displacements for a trapezoidal through-thickness shape of solid-shell elements is assessed. This test is run with the EADG enhancement (T4,$\mathbf{G}^T$).

The directors of the trapezoidal mesh are in the X0Z-plane and the load P is parallel to the 0Z-axis. The data is as

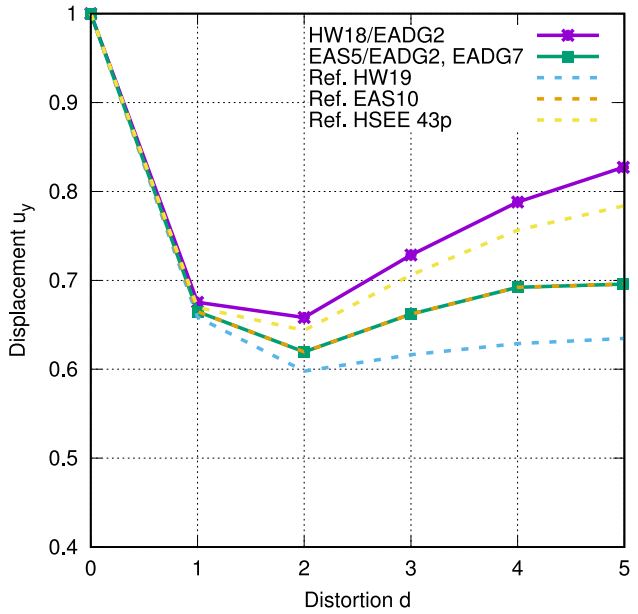

Fig. 7 Two-element distortion test. In-plane bending. EADG (T4,$\mathbf{G}/\mathbf{G}^T$)

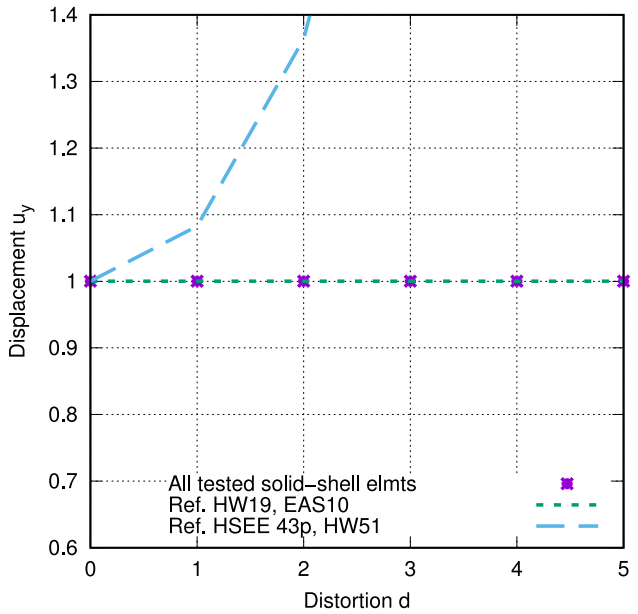

Fig. 8 Two-element distortion test. Out-of-plane bending. EADG (T4,$\mathbf{G}/\mathbf{G}^T$)

follows: $E = 10^7$, $\nu = 0.3$, the length $L = 6$, the thickness $h = 0.2$ and the width in the 0Y direction $w = 0.1$ (Fig. 9).

The vertical displacement u_z at node A is presented in Table 3. For the rectangular mesh, all the tested and reference solid-shell elements perform well and the relative errors are below 0.78%. For the trapezoidal mesh, the tested elements perform similarly as for the rectangular mesh. The elements EAS5/EADG2 and EADG7 are very accurate, with an error of just 0.08% for both meshes. The reference modified 3D TSCG12 performs well with the rectangular mesh but is locked for the trapezoidal mesh.

5.2.5 Curved 3D cantilever

Skew nodal "directors" of solid-shell elements do affect the accuracy of the solution, especially when the thickness h diminishes.

The curved 3D cantilever is fixed at one end and loaded by a moment M_z at the other, see Fig. 10. The data is as follows: $E = 2 \cdot 10^5$, $\nu = 0$, width $b = 0.025$ and radius of curvature $R = 0.1$, thickness $h = 10^{-2}$ $(R/h = 10)$. The nodes shown in Fig. 10 are doubled in the through-thickness direction to created a mesh for the 8-node elements. Six-element mesh is used.

The regular mesh of Fig. 10 is used in the circumferential direction. Note that the distorted mesh in this direction is tested in Koschnick et al. [27] and subsequently in [52]. In the through-thickness direction, two meshes are tested; one with the radial and the other with skew nodal "directors", where the angle $\varphi \approx 35^o$, see Fig. 11.

The displacements u_y at point A (node 1) obtained in the linear analysis are shown in Table 4, where also the relative errors [in %] are given. The EADG (T4,$\mathbf{G}^T$) enhancement is used. The results for (T4,$\mathbf{G}$) are identical.

The reference analytical displacement for a curved beam is $u_y^{\text{ana}} = M_z R^2/EI$, where $I = bh^3/12$ is the moment of inertia. The external moment $M_z = (R/h)^{-3}$ is applied to the 8-node solid-shell element as two pairs of opposite tangent forces $P = M_z/h/2$. For the given data, the reference value is $u_y^{\text{ana}} = 12/(bER) = 0.024$.

Fig. 9 Straight cantilever by trapezoidal elements. Geometry and meshes

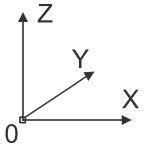

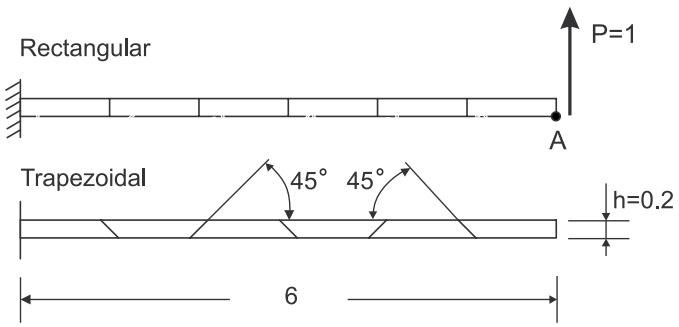

Table 3 Straight cantilever of trapezoidal elements

Element	Vertical displacement $u_y \times 10$ and its relative error [in %]	
	Rectangular mesh	Trapezoidal mesh
Tested new solid-shell		
HW18/EADG2	1.0726 (− 0.78%)	1.0719 (− 0.84%)
EAS5/EADG2	1.0801 (− 0.08%)	1.0801 (− 0.08%)
EADG7	1.0801 (− 0.08%)	1.0801 (− 0.08%)
Ref. solid-shell		
HW19	1.0726 (− 0.78%)	1.0719 (− 0.84%)
EAS10	1.0726 (− 0.78%)	1.0719 (− 0.84%)
HSEE	1.0728 (− 0.76%)	1.1312 (4.64%)
Ref. 8-node 3D solid		
3D TSCG12* with $\mathbf{H}_b^T$	1.0719 (− 0.84%)	0.2413 (− 77.68%)
Reference [28]	1.081	

Linear results. EADG (T4,$\mathbf{G}^T$)

*Modified (local reference basis as for solid-shells and $2 \times 2 \times 2$ Gauss Points)

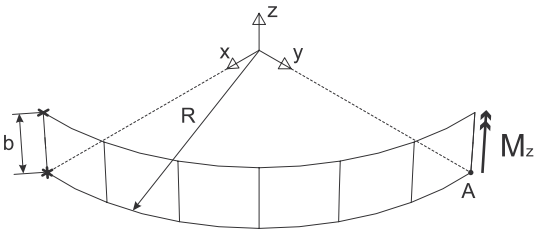

Fig. 10 Curved 3D cantilever. Initial geometry and load. Regular mesh in circumferential direction

For the radial nodal "directors", all the tested solid-shell elements are equally accurate, with an error of 1.81%. For the skew "directors", the errors approximately double this, and the differences between the tested elements are small.

5.3 Non-linear tests

5.3.1 Cook's membrane

In the Cook's membrane test [7], the elements are skewed and tapered and the in-plane shear deformation dominates. The membrane is clamped at one end, while a uniformly distributed vertical load P is applied at the other end, see Fig. 12a. The nodes shown in this figure are doubled in the 0Z direction to obtain the mesh for the 8-node solid-shell elements and the reference 3D solid element. The nodal "directors" are in the 0Z direction.

A. Linear tests. SVK material The purpose of this test is twofold: (1) to compare the accuracy of the tested solid-shell elements, and (2) to check the element EADG7 for various combinations of transformations T1/T2/T3/T4 of Sect. 3 and the form of the matrix $\mathbf{G}/\mathbf{G}^T$.

The data for the SVK material is as follows: $E = 1$, $\nu = 1/3$, and the thickness $h = 1$. Two meshes are used; a coarse 2×2-element mesh and a fine 32×32-element mesh in the X0Y plane. One element is used in the 0Z direction in both cases. The uniformly distributed vertical load $P = +1$ is applied.

The vertical displacements u_y at point A obtained in the linear analysis are presented in Table 5, alongside the relative errors [in %]. For the enhancement (T4,$\mathbf{G}^T$), HW18/EADG2 is the most accurate with an error for the coarse mesh smaller than of the reference HW19. For the fine

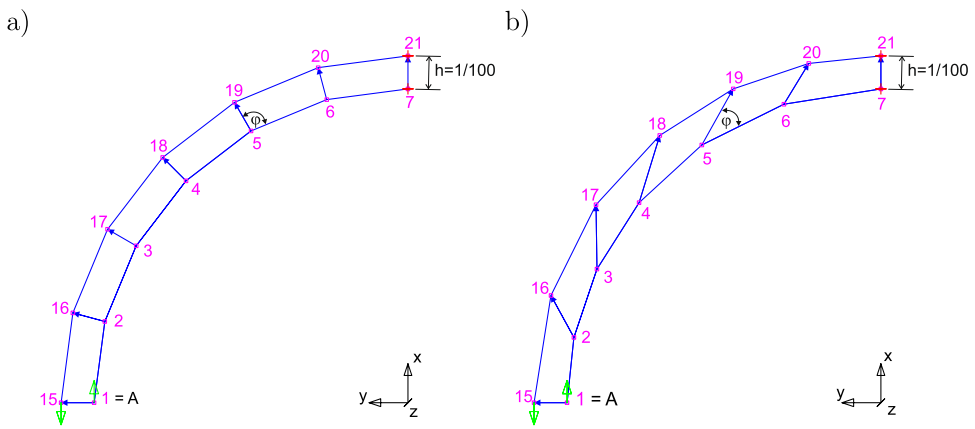

Fig. 11 Curved 3D cantilever. **a** Radial and **b** skew nodal "directors"

Table 4 Curved 3D cantilever

Element	Displacement $u_y \times 100$ and relative error [in %]	
	Radial "directors"	Skew "directors"
Tested new solid-shell		
HW18/EADG2	2.4434 (1.81%)	2.4898 (3.74%)
EAS5/EADG2	2.4434 (1.81%)	2.4884 (3.68%)
EADG7	2.4434 (1.81%)	2.4887 (3.70%)
Ref. solid-shell		
HW19	2.4434 (1.81%)	2.4980 (4.08%)
EAS10	2.4434 (1.81%)	2.4979 (4.08%)
HSEE	2.4618 (2.58%)	2.7033 (12.64%)
Ref. 2D 4-node Plane Stress		
HW14-S, HR5-S [49]	2.3610 (− 1.63%)	2.3832 (− 0.70%)
Ref. 8-node 3D solid		
3D TSCG12* with $\mathbf{H}_b^T$ [24]	2.3495 (− 2.10%)	2.2434 (6.53%)
Ref. beam solution [28]	2.4000	

Displacement u_y at node A and its relative error [in %] for radial and skew nodal "directors". EADG (T4,$\mathbf{G}/\mathbf{G}^{\mathrm{T}}$)

*Modified (local reference basis as for solid-shells and $2 \times 2 \times 2$ Gauss Points)

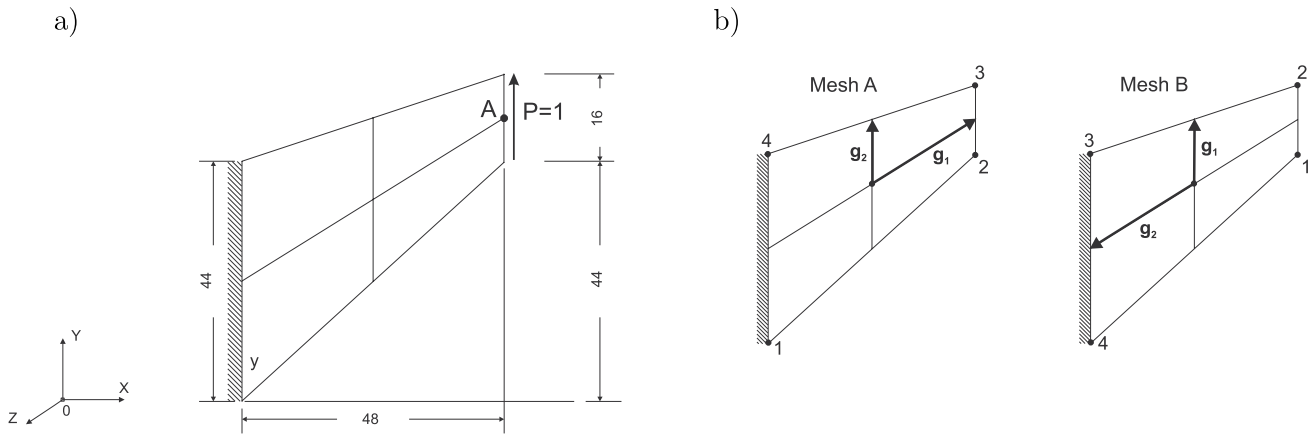

Fig. 12 Cook's membrane. **a** Initial geometry and load. **b** Two meshes with different orders of nodes ($\mathbf{g}_1$ and $\mathbf{g}_2$ are natural vectors at the master block's center.)

mesh, all of the tested elements are equally accurate with an error of 0.31%.

Next, for the element EADG7, all combinations of transformations T1/T2/T3/T4 and the matrix $\mathbf{G}/\mathbf{G}^T$ were tested. In linear tests, T2 and T4 are identical because then $\mathbf{J}_0^{\mathrm{curr}}$ is reduced to $\mathbf{J}_0$, see Eq. (31). For $\mathbf{G}$ and $\mathbf{G}^T$, the results are identical because the enhanced linear strain is insensitive to the transposition of $\mathbf{G}$, see Eq. (42). The idea of using $\mathbf{G}^T$ to suppress mesh hourglassing must be discarded for T1 and T3. However it is admissible for T2 and T4; see the results for the element EADG7 in Table 5. Therefore, only the combinations (T2,$\mathbf{G}^T$) and (T4,$\mathbf{G}^T$) are tested in the sequel.

Finally, two different numberings of nodes are used on the master block, from which mesh A and B are generated, see Fig. 12b. The same results for both meshes are obtained as required.

B. Nonlinear tests. Hyperelastic material The solid-shell element EADG7 is tested in the range of large deformations. Either (T2,$\mathbf{G}^T$) or (T4,$\mathbf{G}^T$) variant of the EADG enhancement is used. Two load cases, –P and +P, are studied.

The nodal "directors" are positioned along the 0Z axis (see Fig. 12a) and the displacements u_z are constrained to zero for nodes located at $z = 0$ to prevent out-of-plane buckling. Three $n \times n$-element meshes for $n = 2, 4, 16$ are used, and one element is used through thickness. The standard Newton method and the load increments $\Delta P = \pm 0.01$ are applied. The deformed meshes for loads –P and +P after 320 steps are shown in Fig. 13.

The modified neo-Hookean hyper-elastic material of Eq. (68) is used with the shear modulus $\mu = 0.333355557$ and the bulk modulus $K = 0.166666667 \cdot 10^4$; these values are obtained from $E = 1$ and $\nu = 0.4999$. Additionally, $\beta = -2$ is used.

Table 5 Cook's membrane

Element	Form of EADG	Vertical displacement u_y (error in %)	
		Mesh 2×2	Mesh 32×32
Tested new solid-shell			
HW18/EADG2	(T4,$\mathbf{G}^T$)	21.294 (− 10.57%)	23.884 (0.31%)
EAS5/EADG2	(T4,$\mathbf{G}^T$)	21.076 (− 11.49%)	23.884 (0.31%)
EADG7	(T1/T3,$\mathbf{G}$)	21.076 (− 11.49%)	23.884 (0.31%)
	(T1/T3,$\mathbf{G}^T$)	13.600 (− 42.88%)	23.802 (− 0.03%)
	(T2/T4,$\mathbf{G}/\mathbf{G}^T$)	21.076 (− 11.49%)	23.884 (0.31%)
Ref. solid-shell			
HW19	–	21.126 (− 11.27%)	23.884 (0.31%)
EAS10	–	21.076 (− 11.49%)	23.884 (0.31%)
HSEE	–	21.073 (− 11.49%)	23.884 (0.31%)
Ref. 2D Plane Stress [own]			
2D TSCG6**	$\mathbf{H}_b/\mathbf{H}_b^T$	21.136 (− 11.23%)	23.940 (0.55%)
2D EAS7	–	21.129 (− 11.26%)	23.940 (0.55%)
Ref. 8-node 3D solid			
3D TSCG12* [24]	$\mathbf{H}_b^T$	21.021 (− 11.71%)	23.884 (0.31%)
Ref		23.81	23.81

Linear analysis. Accuracy of elements and effects of various combinations of T1/T2/T3/T4 and $\mathbf{G}/\mathbf{G}^T$

*Modified (local reference basis as for solid-shells and $2 \times 2 \times 2$ Gauss Points) **2D TSCG6 for Plane Stress is analogous to 3D TSCG12 of [24]

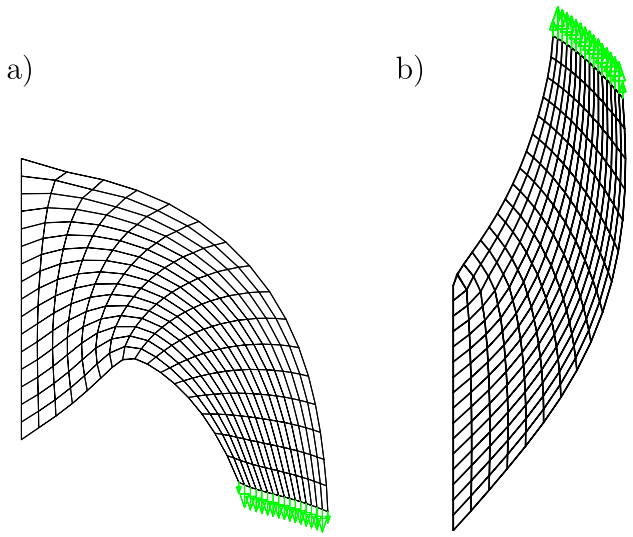

Fig. 13 Cook's membrane. Deformed mesh after 320 steps for load: **a**$-P$,**b**$+P$

The displacements u_x and u_y at node A are shown in Fig. 14. (Node A is positioned as shown in Fig. 12a.) The reference solutions (Ref.) are obtained using the mesh for $n = 16$ and three finite elements: (1) solid-shell element EADG7 with the enhancement (T2,$\mathbf{G}^T$), (2) solid-shell element EADG7 with the enhancement (T4,$\mathbf{G}^T$), (3) solid element 3D TSCG12 with $\mathbf{H}_b^T$ of [24] modified for shell applications as described in the introduction to Sect. 5. For all these elements, the solutions coincide for the selected displacement component and the load case, and are treated as the reference solution.

This example is then run for coarse meshes ($n = 2$ and 4) and the solid-shell element EADG7 either with (T2,$\mathbf{G}^T$) or (T4,$\mathbf{G}^T$). The results are shown in Fig. 14, where the order of the curves, from most to least accurate, is as follows:

(a) For the load −P (Fig. 14a),

$$u_x : (n = 4,\ \mathrm{T2}) = (n = 4,\ \mathrm{T4}),\quad (n = 2,\ \mathrm{T2}),\quad (n = 2,\ \mathrm{T4}),$$
$$u_y : (n = 4,\ \mathrm{T2}),\quad (n = 4,\ \mathrm{T4}),\quad (n = 2,\ \mathrm{T2}),\quad (n = 2,\ \mathrm{T4}).$$

For u_x and $n = 4$, the curves for T2 and T4 coincide, while for u_y, the curve for T2 is slightly more accurate than the one for T4.

(b) For the load +P (Fig. 14b),

$$u_x : (n = 2,\ \mathrm{T4}) = \mathrm{Ref.},\quad (n = 4,\ \mathrm{T4}),\quad (n = 4,\ \mathrm{T2}),\quad (n = 2,\ \mathrm{T2}),$$
$$u_y : (n = 4,\ \mathrm{T4}) = (n = 2,\ \mathrm{T4}) = \mathrm{Ref.},\quad (n = 4,\ \mathrm{T2}),\quad (n = 2,\ \mathrm{T2}).$$

For u_x, the curve $(n = 2,\ \mathrm{T4})$ coincides with the reference curve (Ref.). For u_y, both curves for T4 coincide with the reference one, while those for T2 are less accurate.

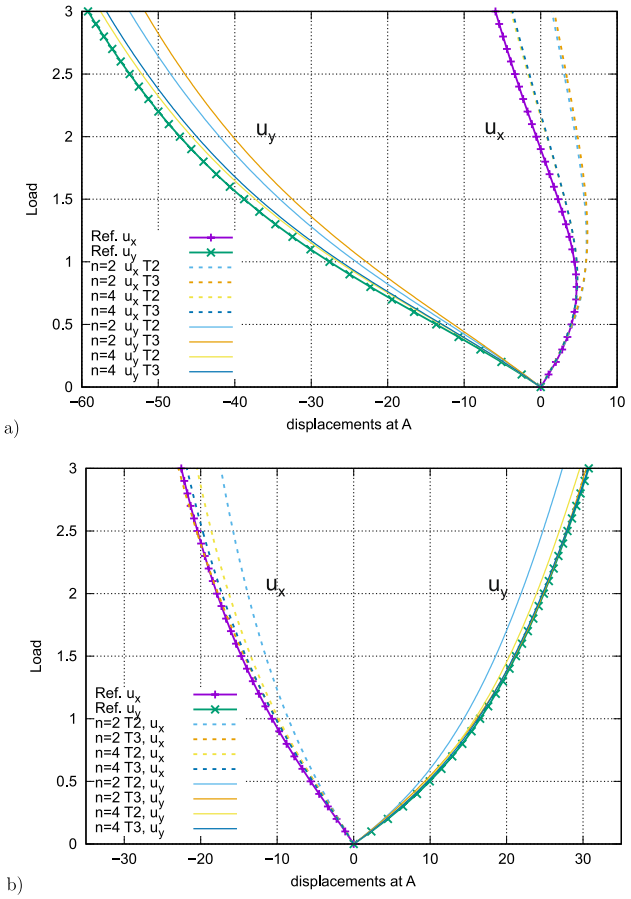

Fig. 14 Cook's membrane. Non-linear solutions for load: **a** $-P$, **b** $+P$. Element EADG7. Enhancement matrix $\mathbf{G}^T$ and transformations T2 and T4 are tested

In summary, the transformation T4 performs very well in this non-linear example. For the load +P, it performs even better than T2, which is used in [25] and [12].

5.3.2 Pinched hemispherical shell with hole

The hemispherical shell with an 18^o hole is loaded by two pairs of equal but opposite external forces, see Fig. 15. The shell undergoes an almost in-extensional deformation, so a membrane locking of solid-shell elements can be detected by this test.

Using the shell's and load's double symmetry, a quarter of the shell is modeled. One element is used through the thickness and three meshes with 8×8, 16×16 and 64×64 elements over the surface. The nodes shown in Fig. 15 are doubled in the through-thickness direction to obtain the mesh for 8-node solid-shell elements. The thickness $h = 0.04$ is used, as in [28].

This test is run for two materials. For the SVK material, $E = 6.825 \times 10^7$ and $\nu = 0.3$. For these values the bulk modulus is $K = 5.6875 \times 10^7$ and the shear modulus is $\mu = 2.625 \times 10^7$. The latter constants are used for the hyperelastic material of Eq. (68). All new elements, i.e. HW18/EADG2, EAS5/EADG2 and EADG7, are run with the EADG (T4,$\mathbf{G}^T$) enhancement.

The results of the linear analyses are given in Table 6, where the inward displacement u_y under the force $P = 1$ at the inner node is reported. The conclusions are as follows:

1. For all new solid-shell elements, the obtained displacements are identical to those yielded by the reference solid-shell elements HW19 and EAS10, but slightly differ from those yielded by the reference HSEE.
2. The results for reference 8-node 3D solid elements are less accurate for the 8×8 and 16×16-element meshes than the ones for the solid-shell elements. For the dense 64×64-element mesh, the results have the same relative error.

The non-linear analyses are performed using the 16×16 -element mesh and the Newton method. The solution curves are shown in Fig. 16. For all new solid-shell elements and both materials, linear elastic (SVK) and hyperelastic, the curves fully coincide over the whole load range, and are very close to that for the reference 4-node shell element HW47 with 6 dofs/node and the RBF correction of [50].

The solutions obtained by two versions of the 3D TSCG12 element of Korelc et al. [24] are also shown in Fig. 16. The standard version uses the special 9-point integration rule ($2 \times 2 \times 2 + \text{center}$) of [40], while the modified version uses the $2 \times 2 \times 2$ Gauss integration and the local reference basis, see the introduction to Sect. 5. The modified

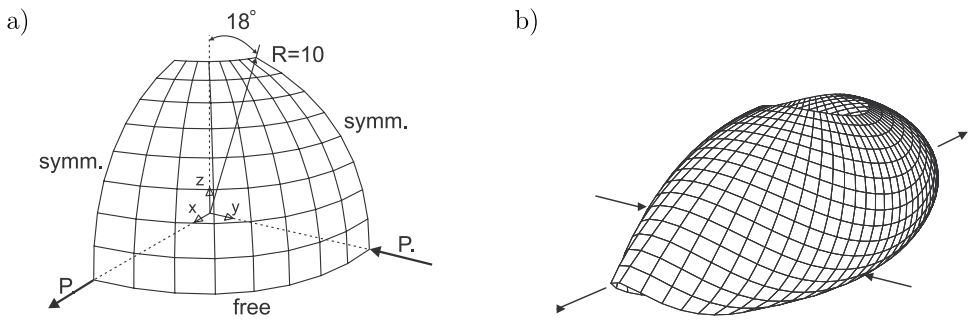

Fig. 15 Pinched hemispherical shell with hole. **a** Geometry and boundary conditions. **b** Deformed shape

Table 6 Pinched hemispherical shell with hole

Element	Displacement $-u_y \times 100$ and relative error [in %]		
	8×8	16×16	64×64
Tested new solid-shell			
All new elmts	9.4306 (0.33%)	9.3446 (− 0.59%)	9.3548 (− 0.48%)
Ref. solid-shell			
HW19, EAS10	9.4306 (0.33%)	9.3446 (− 0.59%)	9.3548 (− 0.48%)
HSEE	9.4505 (0.54%)	9.3511 (− 0.52%)	9.3555 (− 0.43%)
Ref. 8-node 3D solid			
3D.HW51	6.9776 (6.14%)	9.2594 (− 1.49%)	9.3545 (− 0.48%)
3D.EAS-30 [1]	6.9776 (6.14%)	9.2594 (− 1.49%)	9.3545 (− 0.48%)
3D TSCG12* with $\mathbf{H}_b^T$	4.5510 (− 51.6%)	8.8978 (− 5.34%)	9.3546 (− 0.48%)
Reference [28]		9.4000	

Linear solutions for 3 meshes. SVK material. $h = 0.04$. EADG (T4,$\mathbf{G}^T$)

*Modified (local reference basis as for solid-shells and $2 \times 2 \times 2$ Gauss Points)

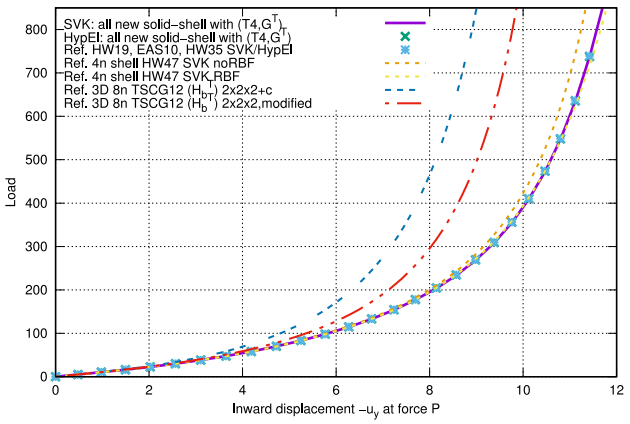

Fig. 16 Pinched hemispherical shell with hole. Non-linear solutions for SVK and hyperelastic material. Mesh 16×16 elements. $h = 0.04$

Table 7 Pinched hemispherical shell with hole

Element	Max ΔP	No. of iterations
Tested new solid-shell		
HW18/EADG2	0.5	24
EAS5/EADG2	0.4	28
EADG7	0.4	28
Ref. solid-shell		
HW19	0.5	24
EAS10	0.4	28
HSEE	4.4	14
HW35 [52]	3.5	11

One-step non-linear test. $h = 0.01$

version is more accurate than the standard one, with the 8% error of the inward displacement at $P = 800$.

One-step non-linear test. The non-linear finite elements can differ in the radius and rate of convergence of the Newton method. These can be characterized by the maximum ΔP for which the method converges and by the number of iterations performed.

In this test only one step is performed and the maximum load for which the Newton method converges is found by successively increasing the initial ΔP by 0.1. The shell and load of Fig. 15a are analyzed using the 16×16-element mesh and the thickness $h = 0.01$ for the SVK material. The results obtained using the EADG enhancement with (T4,$\mathbf{G}^T$) are presented in Table 7.

The tested new solid-shell elements inherit the radius of convergence (Max ΔP) and the number of iterations from their parent elements, i.e. HW18/EADG2 from the reference HW19, and EAS5/EADG2 from the reference EAS10. The reference solid-shell elements HSEE and HW35 of [52] converge for a larger Max ΔP and in fewer iterations, but involve more additional parameters.

5.3.3 Twisted beam

The initial geometry of the beam is twisted so all the elements are warped (non-flat) but the initial strains are equal to zero. The beam is clamped at one end and loaded by a force P_y at the other end, see Fig. 17a. The SVK (linear, elastic) material is used with $E = 2.9 \times 10^7$ and $\nu = 0.22$. The other data is as follows: the length $L = 12$, the width $w = 1.1$ and the twist angle is 90°, as in [28].

In the computations, a 4×24-element mesh of the 8-node solid-shell elements and a small thickness $h = 0.0032$ are used. One element is used through the thickness. Regarding the reference shell elements (Reissner-Mindlin with 6 dofs/node), the 4×24-element mesh is used for the 4-node HW47 and the 2×12-element mesh for the 9-node MITC9i. All new solid-shell elements use the EADG (T4,$\mathbf{G}^T$) enhancement.

The results of a linear analysis for $P_y = 10^{-6}$ are presented in Table 8, where the $u_y \times 10^3$ displacement at point A and its relative error are shown. The tested new solid-shell elements, i.e. HW18/EADG2, EAS5/EADG2 and EADG7,

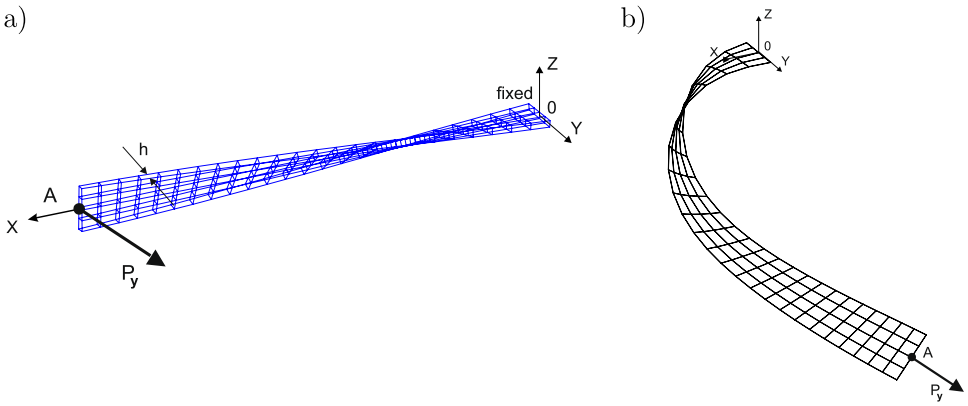

Fig. 17 Twisted beam. **a** Initial mesh and load. **b** Deformed mesh at $P_y = 0.1$

Table 8 Twisted beam

Element	Form of EADG	$u_y \times 10^3$	Relative error
Tested new solid-shell			
HW18/EADG2	(T4, $\mathbf{G}^T$)	1.2934	− 0.05%
EAS5/EADG2	(T4, $\mathbf{G}^T$)	1.2916	− 0.19%
EADG7	(T4, $\mathbf{G}^T$)	1.2924	− 0.12%
	(T4, $\mathbf{G}$)	1.2927	− 0.10%
Ref. solid-shell			
HW19	–	1.2900	− 0.31%
EAS10	–	1.2918	− 0.17%
HSEE	–	1.2915	− 0.19%
Ref. 8-node 3D solid			
3D TSCG12*	$\mathbf{H}_b^T$	0.5339	− 58.74%
Ref. shell 6 dofs/node			
4-node HW47 [50]	–	1.2877	− 0.49%
9-node MITC9i [51]	–	1.2948	0.06%
Reference [28]		1.2940	

Linear results for out-of-plane load $P_y = 10^{-6}$

*Modified (local reference basis as for solid-shells and $2 \times 2 \times 2$ Gauss Points)

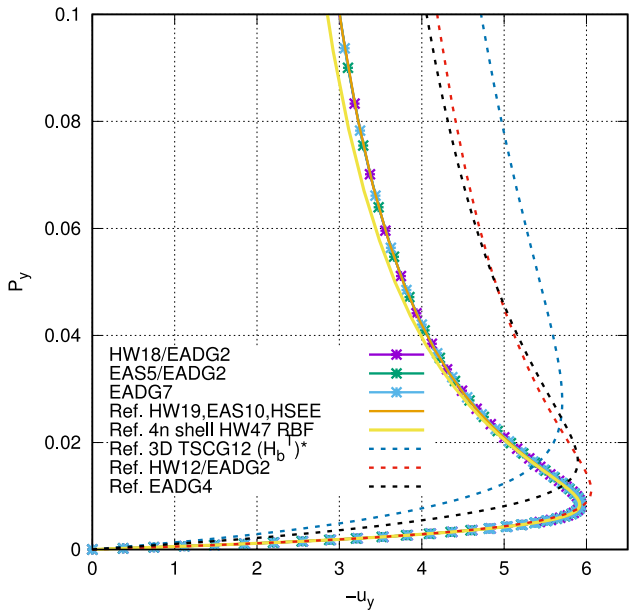

Fig. 18 Twisted beam. Out-of-plane load. Non-linear solutions. The elements yielding inaccurate solutions (dotted lines) are described in the text. EADG (T4,$\mathbf{G}^T$)

have the accuracy similar to the reference elements HW19, EAS10 and HSEE.

The non-linear load-deflection curves are obtained for $\Delta P_y = 10^{-4}$ using the arc-length method and are shown in Fig. 18. The displacement u_y at point A is monitored. The tested new solid-shell elements yield the solutions that coincide with those for the reference solid-shell elements. They are only minimally stiffer than the solution for the reference 4-node shell HW47 with 6 dofs/node run with the RBF correction.

In summary, the analyzed shell is very slender ($L/h = 3750$) but all the new solid-shell elements provide results of very good accuracy.

Remark. Three curves in Fig. 18 are inaccurate; for the reference solid element 3D TSCG12 (modified) and for two reference solid-shell elements HW12/EADG2 and EADG4, which have not been characterized yet. The element HW12/EADG2 is obtained from HW18/EADG2 by removing the assumed stress S_{12}^{0*} and the assumed strain E_{12}^{0*} from Eq. (55), and using the compatible strain E_{12}^{0} in the strain energy $\mathcal{W}$ instead. The element EADG4 is formulated as the element EADG7 but is based on the EADG4 representation of Eq. (63).

5.3.4 Compression of a nearly-incompressible block

The purpose of this test is to find the critical compressive strain for the tested new solid-shell elements and to check whether mesh hourglassing occurs at this strain. To remove hourglassing, the EADG (T4,$\mathbf{G}^T$) enhancement is used.

The $1 \times 1 \times 1$ block is supported at the bottom in the vertical direction and compressed by a sequence of vertical displacement increments $\Delta \mathrm{v} = 0.001$ applied at the top, see Fig. 19. The mesh of $10 \times 10 \times 1$ elements is used, with one

element in the direction normal to the plane of the figure. The displacements in this direction are set to zero.

The modified neo-Hookean hyper-elastic material model is used, with the strain energy function $\mathcal{W}$ for the volumetric/isochoric split of the deformation gradient $\mathbf{F}$,

$$\mathcal{W} = \frac{\mu}{2}\left(J^{-2/3}\mathrm{tr}\ \mathbf{C} - 3\right) + \frac{K}{\beta^2}\left(J^{-\beta} - 1 + \beta \ln J\right), \qquad (68)$$

where $\mathbf{C} = \mathbf{F}^T\mathbf{F}$ is the right Cauchy-Green deformation tensor and $J = \det \mathbf{F}$. The material data is as follows: the shear modulus $\mu = 20$, the bulk modulus $K = 4 \cdot 10^5$ and the dimensionless parameter $\beta = -2$. For these μ and K, we obtain $E = 59.999$ and $\nu = 0.499975$. For these values, K plays the role of a penalty multiplier for the second term in Eq. (68). The transverse shear correction factor $k = 1$.

The procedure is as follows: The Newton method is used to solve the equilibrium equations for each increment Δv and the 5 lowest eigenvalues of the tangent stiffness matrix are computed at converged configurations using ARPACK .[1] For the lowest eigenvalue equal to zero, the corresponding scaled eigenvector is then plotted on the current mesh.

For the compression in the tangent plane of the solid-shell elements, i.e. when the nodal "directors" are perpendicular to the plane of Fig. 19, the obtained critical strains (first zero eigenvalue) are given in Table 9. The EADG enhancement is used with the transformation rule T4 and either $\mathbf{G^T}$ or $\mathbf{G}$. The last column indicates whether hourglassing appears at the critical strain. We note that:

1. For $\mathbf{G^T}$, the same critical strain 0.526 is obtained for all the tested new solid-shell elements, and the mesh hourglassing at this strain is suppressed.
2. For $\mathbf{G}$, the critical strain is smaller, equal to 0.417, and the hourglassing is present at the critical strain for all elements. The same value and hourglassing are obtained for the reference solid-shell elements HW19 and EAS10.

The lowest eigenvalues of the stiffness tangent matrix are shown vs. the vertical displacement v in Fig. 20. For the tested new solid-shell elements:

1. All the solutions for $\mathbf{G}^T$ coincide and all the solutions for $\mathbf{G}$ coincide, so only two curves are depicted for these two cases.
2. The curves for solid-shell elements correspond to the curves for the reference 3D TSCG12 element in the standard or modified form, using either $\mathbf{H}_b^T$ or $\mathbf{H}_b$.

[1] ARPACK is a numerical software library for solving large scale eigenvalue problems (www.arpack.org).

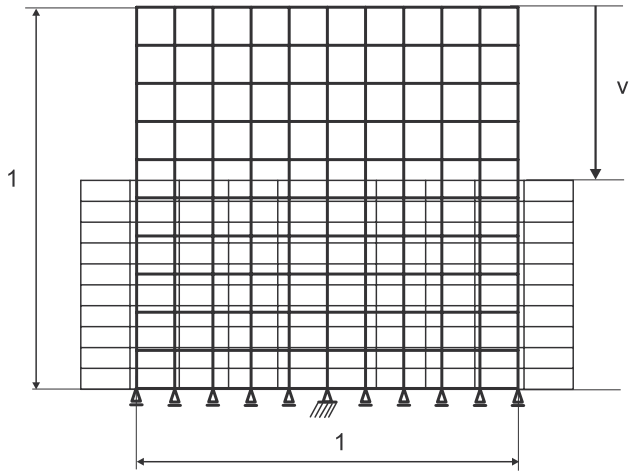

Fig. 19 Compression of nearly-incompressible block. Problem definition

Table 9 Compression of a nearly-incompressible block

Element	Form of EADG	In-plane compression	
		Critical strain	Hourglassing
Tested new solid-shell			
HW18/EADG2	(T4,$\mathbf{G}^T$)	0.526	No
	(T4,$\mathbf{G}$)	0.417	Yes
EAS5/EADG2	(T4,$\mathbf{G}^T$)	0.526	No
	(T4,$\mathbf{G}$)	0.417	Yes
EADG7	(T4,$\mathbf{G}^T$)	0.526	No
	(T4,$\mathbf{G}$)	0.417	Yes
Ref. solid-shell (no EADG)			
HW19	–	0.416	Yes
EAS10	–	0.416	Yes
HSEE	–	0.373	Yes
HW51	–	0.297/0.309	No
Ref. 8-node 3D solid			
3D TSCG12*	$\mathbf{H}_b^T$	0.513	No
	$\mathbf{H}_b$	0.372	Yes

Critical strains and hourglassing

*Modified (local reference basis as for solid-shells and $2 \times 2 \times 2$ Gauss Points)

The computed eigenvectors at the first zero eigenvalue are re-scaled and superimposed on the deformed mesh. Examples of a mesh with and without hourglassing are shown in Fig. 21.

Remark For the normal compression of the tested new solid-shell elements, i.e. when the nodal "directors" are within the plane of Fig. 19, the obtained critical strain is 0.115 and the mesh hourglassing appears for all elements. Similar values are obtained for the reference (parent) solid-shell elements HW19, EAS10 and HSEE, see Table 12 in [52].

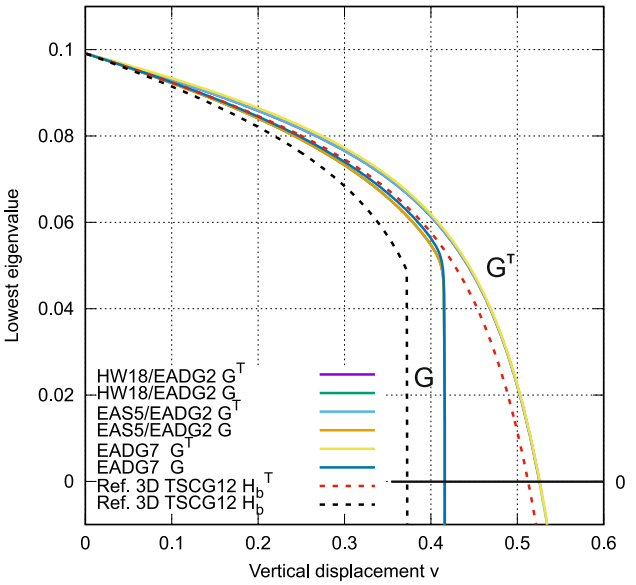

Fig. 20 Compression of a nearly-incompressible block in the tangent plane of elements. Lowest eigenvalue of the tested new elements using EADG (T4, $\mathbf{G}/\mathbf{G}^T$)

6 Final remarks

Three eight-node (hexahedron) solid-shell elements have been proposed and tested in the current paper. Their formulation eliminates mesh hourglassing at the bifurcation point for a nearly incompressible hyperelastic material under compression. The elements have correct rank, pass the membrane and bending patch tests and are free from the curvature thickness, transverse shear and volumetric locking.

1. Mesh hourglassing is suppressed by transposing the matrix $\mathbf{G}$ in the enhancement of the deformation gradient $\mathbf{F}$, as for a 4-node 2D plane strain element in [25] and [12].

   (a) The 2-parameter representation EADG2 is proposed as a means to suppress hourglassing in the elements HW18/EADG2 and EAS5/EADG2. Note that other modifications are also required to obtain a correct form of these elements from their parent elements, see Sects. 4.1.2 and 4.2.2 for details.

   (b) The element EADG7 inherits the feature of suppressing the mesh hourglassing by transposing matrix $\mathbf{G}$ from its parent element EADG4. Three $\xi\eta$ -modes are incorporated into the EADG7 element, see Eq. (64), to eliminate one of the spurious large eigenvalues for the incompressible material and to improve bending behavior.

2. With regard to the transformation rules for the EADG enhancement, we propose and test the rule designated T4 in Sect. 3. T4 involves $(\mathbf{J}_0^{\text{curr}})^{-T}$, where $\mathbf{J}_0^{\text{curr}}$ is the current Jacobian at the element's center, and it is an alternative to the three other transformations, designated T1, T2 and T3, that exist in the literature. It is found that the transposition of matrix $\mathbf{G}$ works well with T2 and the proposed T4, but not with T1 and T3. Regarding the performance of the transformation T4,

   (a) In linear tests, the results for $\mathbf{G}$ and $\mathbf{G}^T$ are equal because the enhanced linear strain is insensitive to the transposition of $\mathbf{G}$, see Eq. (42) and Table 5.

   (b) In non-linear tests, distinct solutions are obtained when using $\mathbf{G}$ and $\mathbf{G}^T$. For the Cook's membrane (Sect. 5.3.1), T4 performs very well and for the load +P even better than T2. For the compression of a nearly-incompressible block (Sect. 5.3.4), there is no mesh hourglassing under tangent compression at the critical strain for the EADG enhancement with (T4,$\mathbf{G}^T$).

Furthermore, in terms of the accuracy of the solutions in the tests unrelated to hourglassing, the three proposed elements perform very well, i.e. they perform either similarly to or better than their parent elements. This validates the proposed changes and provides an argument for using these elements in analyses of elastic single- and multi-layer shells. Further research is planned to verify their performance also for elasto-plastic materials.

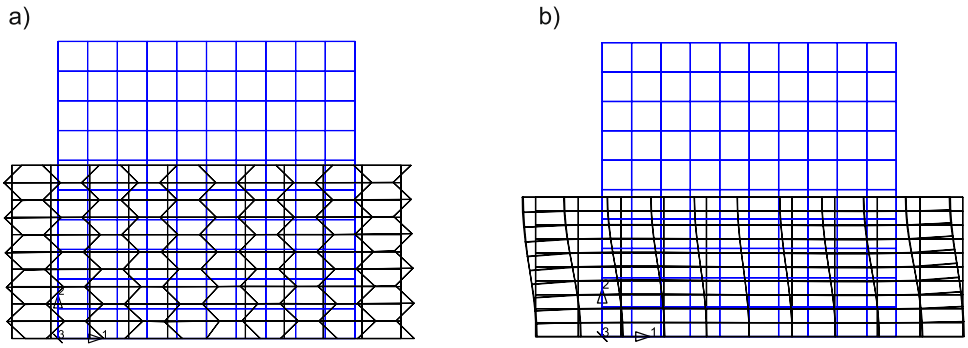

Fig. 21 Compression of a nearly-incompressible block. Eigenvectors for the lowest zero eigenvalue are superimposed on the mesh and show: **a** hourglassing for $\mathbf{G}$, **b** no hourglassing for $\mathbf{G}^T$

Appendix 1: Transformation operators for strain and stress vectors

Because of the symmetry of strain and stress tensors, instead of matrices we can use the vectors of their components

$$\begin{aligned}\mathbf{E}_{\mathrm{v}} &\doteq [E_{11}, E_{22}, E_{33},\ 2E_{12}, 2E_{13}, 2E_{23}]^T,\\ \mathbf{S}_{\mathrm{v}} &\doteq [S_{11}, S_{22}, S_{33},\ S_{12}, S_{13}, S_{23}]^T,\end{aligned} \tag{A1}$$

and define the transformation matrices to obtain the components in another basis. Let us define the transformation matrix

$$\mathbf{T} \doteq \begin{bmatrix} J_{11}^2 & J_{12}^2 & J_{13}^2 & aJ_{11}J_{12} & aJ_{11}J_{13} & aJ_{12}J_{13} \\ J_{21}^2 & J_{22}^2 & J_{23}^2 & aJ_{21}J_{22} & aJ_{21}J_{23} & aJ_{22}J_{23} \\ J_{31}^2 & J_{32}^2 & J_{33}^2 & aJ_{31}J_{32} & aJ_{31}J_{33} & aJ_{32}J_{33} \\ bJ_{11}J_{21} & bJ_{12}J_{22} & bJ_{13}J_{23} & J_{11}J_{22}+J_{12}J_{21} & J_{11}J_{23}+J_{13}J_{21} & J_{12}J_{23}+J_{13}J_{22} \\ bJ_{11}J_{31} & bJ_{12}J_{32} & bJ_{13}J_{33} & J_{11}J_{32}+J_{12}J_{31} & J_{11}J_{33}+J_{13}J_{31} & J_{12}J_{33}+J_{13}J_{32} \\ bJ_{21}J_{31} & bJ_{22}J_{32} & bJ_{23}J_{33} & J_{21}J_{32}+J_{22}J_{31} & J_{21}J_{33}+J_{23}J_{31} & J_{22}J_{33}+J_{23}J_{32} \end{bmatrix}, \tag{A2}$$

where $J_{ik} = \mathbf{g}_i \cdot \mathbf{i}_k^0$ $(i,k = 1,2,3)$ are the components of the Jacobian $\mathbf{J}$ and a, b are scalars. To perform the transformations between the contravariant (CTV) components and the Cartesian (CART) components of vectors (69), we define two operators

$$\mathbf{T}_{\mathrm{E}} \doteq \mathbf{T}(a=1, b=2) \quad \text{and} \quad \mathbf{T}_{\mathrm{S}} \doteq \mathbf{T}(a=2, b=1). \tag{A3}$$

The use of these operators is equivalent to the matrix operations, as specified below.

The CTV $\rightarrow$ CART transformation of components of strain can be written either as

$$\mathbf{E}^{\mathrm{CART}} = \mathbf{J}\,\mathbf{E}^{\mathrm{CTV}}\mathbf{J}^T \quad \text{or} \quad \mathbf{E}_{\mathrm{v}}^{\mathrm{CART}} = \mathbf{T}_{\mathrm{E}}\,\mathbf{E}_{\mathrm{v}}^{\mathrm{CTV}}. \tag{A4}$$

We can check their equivalence, i.e. $\left(\mathbf{E}^{\mathrm{CART}}\right)_{\mathrm{v}} = \mathbf{E}_{\mathrm{v}}^{\mathrm{CART}}$, where $(\cdot)_{\mathrm{v}}$ designates the operation of taking the components of a matrix in a proper order to obtain the strain vector of Eq. (69). Analogous equivalent relations for components of stress are,

$$\mathbf{S}^{\mathrm{CART}} = \mathbf{J}\,\mathbf{S}^{\mathrm{CTV}}\mathbf{J}^T \quad \text{or} \quad \mathbf{S}_{\mathrm{v}}^{\mathrm{CART}} = \mathbf{T}_{\mathrm{S}}\,\mathbf{S}_{\mathrm{v}}^{\mathrm{CTV}}. \tag{A5}$$

The modified versions of the above transformations are used in solid-shell elements in [23] and [52], different in each of these papers. Various rules for the assumed strains are tested and compared for 4-node 2D Hu–Washizu elements in [53].

References

1. Andelfinger U, Ramm E (1993) EAS-elements for 2D- and 3D-, plate and shell structures and their equivalence to HR-elements. Int J Numer Methods Eng 36:1311–1337
2. Areias PM, de Sá JMC, António CC, Fernandes AA (2003) Analysis of 3D problems using a new enhanced strain hexahedral element. J Numer Methods Eng 58(11):1637–1682
3. Armero F (2000) On the locking and stability of finite elements in finite deformation plane strain problems. Comput Struct 75:261–290
4. Belytschko T, Ong JSJ, Liu WK, Kennedy JM (1984) Hourglass control in linear and nonlinear problems. Comput Methods Appl Mech Eng 43(3):251–276
5. Betsch P, Stein E (1995) An assumed strain approach avoiding artificial thickness straining for a non-linear 4-node shell element. Commun Numer Methods Eng 11:899–909
6. Büchter N, Ramm E, Roehl D (1994) Three-dimensional extension of nonlinear shell formulation based on the enhanced assumed strain concept. J Numer Methods Eng 37:2551–2568
7. Cook RD (1987) A plane hybrid element with rotational d.o.f. and adjustable stiffness. J Numer Methods Eng 24:1499–1508
8. Crisfield MA, Moita GF, Jelenic G, Lyons LPR (1995) Enhanced lower-order element formulation for large strains. Comput Mech 17:62–73
9. de Souza Neto EA, Peric D, Huang GC, Owen DRJ (1995) Remarks on the stability of enhanced strain elements in finite elasticity and elastoplasticity. In Computational Plasticity-Fundamentals and

Applications; Part I, Owen D.R.J., Onate E., Hinton E. (eds). Pineridge Press: Swansea
10. Dvorkin EN, Bathe K-J (1984) A continuum mechanics based four-node shell element for general nonlinear analysis. Eng Comput 1:77–88
11. Eidel B, Gruttmann F (2003) Elastoplastic orthotropy at finite strains: multiplicative formulation and numerical implementation. Comput Mater Sci 28:732–742
12. Glaser S, Armero F (1997) On the formulation of enhanced strain finite elements in finite deformations. Eng Comput 14(7):759–791
13. Gruttmann F, Wagner W (2013) A coupled two-scale shell model with application to layered structures. J Numer Methods Eng 94:1233–1254
14. Gruttmann F, Wagner W (2017) Shear correction factors for layered plates and shells. Comput Mech 59(1):129–146
15. Gruttmann F, Wagner W (2020) An advanced shell model for the analysis of geometrical and material nonlinear shells. Comput Mech 66:1353–1376
16. Gruttmann F, Wagner W (2024) A FE2 shell model with periodic boundary conditions for thin and thick shells. J Numer Methods Eng 125(11):e7433
17. Gruttmann F, Wagner W (2025) A nonlinear 4-node shell element with one point quadrature and stabilization based on a Hu–Washizu variational formulation. Comput Mech 76:613–633
18. Harnau M, Schweitzerhof K, Hauptmann R (2000) On solid-shell elements with linear and quadratic shape functions for small and large displacements. In: ECCOMAS congress, Barcelona 11–14 Sept 2000, pp 1–27
19. Hauptmann R, Doll S, Harnau M, Schweizerhof K (2001) "Solid-shell'' elements with linear and quadratic shape functions at large deformations with nearly incompressible materials. Computers & Structures 79:1671–85
20. Hauptmann R, Schweizerhof K (2000) Doll S: extension of the solid-shell concept for large elastic and large elastoplastic deformations. J Numer Methods Eng 49:1121–41
21. Jarzebski P, Wisniewski K, Taylor RL (2015) On parallelization of the loop over elements in FEAP. Comput Mech 56(1):77–86
22. Klinkel S, Gruttmann F, Wagner W (1999) A continuum based three-dimensional shell element for laminated structures. Computers & Structures 71(1):43–62
23. Klinkel S, Gruttmann F, Wagner W (2006) A robust non-linear solid shell element based on a mixed variational formulation. Comput Methods Appl Mech Eng 195:179–201
24. Korelc J, Solinc U, Wriggers P (2010) An improved EAS brick element for finite deformation. Comput Mech 46:641–659
25. Korelc J, Wriggers P (1996) Consistent gradient formulation for a stable enhanced strain method for large deformations. Eng Comput 13(1):103–123
26. Korelc J, Wriggers P (2016) Automation of finite element methods. Springer, Cham
27. Koschnick F, Bischoff GA, Camprubi N, Bletzinger KU (2005) The discrete strain gap method and membrane locking. Comput Methods Appl Mech Eng 194:2444–2463
28. MacNeal RH, Harder RL (1985) A proposed standard set of problems to test finite element accuracy. Finite Elem Anal Des 1:3–20
29. Nagtegaal JC, Parks DM, Rice JR (1974) On numerically accurate finite element solutions in the fully plastic range 4:153–177
30. Nagtegaal JC, Fox DD (1996) Using assumed enhanced strain elements for large compressive deformation. Int J Solids Structures 33(20–22):3151–3159
31. Pantuso D, Bathe KJ (1997) On the stability of mixed finite elements in large strain analysis of incompressible solids. Finite Elem Anal Des 28(2):83–104
32. Pfefferkorn R, Betsch P (2019) On transformations and shape functions for enhanced assumed strain elements. Int J Numer Methods Eng 120:231–261
33. Pfefferkorn R, Betsch P (2023) Hourglassing- and locking-free mesh distortion insensitive Petrov-Ggalerkin EAS element for large deformation solid mechanics. J Numer Methods Eng 124(6):1307–1343
34. Pian THH, Sumihara K (1984) Rational approach for assumed stress finite elements. J Numer Methods Eng 20:1685–1695
35. Reese S, Wriggers P (2000) A stabilization technique to avoid hourglassing in finite elasticity. Int J Numer Methods Eng 48:79–109
36. Reese S (2005) On a physically stabilized one point finite element formulation for three-dimensional finite elasto-plasticity. Comput Methods Appl Mech Eng 194(45):4685–4715
37. Schröder J, Gruttmann F, Löblein J (2002) A simple orthotropic finite elasto-plasticity model based on generalized stress-strain measures. Comput Mech 30:48–64
38. Schwarze K, Reese S (2011) A reduced integration solid-shell finite element based on the EAS and the ANS concept–Large deformation problems. Int J Numer Methods Eng 85:289–329
39. Simo JC, Armero F (1992) Geometrically non-linear enhanced strain mixed methods and the method of incompatible modes. Comput Methods Appl Mech Eng 33:1413–1449
40. Simo JC, Armero F, Taylor RL (1993) Improved version of assumed enhanced strain tri-linear element for 3D finite deformation problems. Comput Methods Appl Mech Eng 73:53–92
41. Simo JC, Rifai MS (1990) A class of mixed assumed strain methods and the method of incompatible modes. Int J Numer Methods Eng 29:1595–1638
42. Taylor RL, Beresford PJ, Wilson EL (1976) A non-conforming element for stress analysis. Int J Numer Methods Eng 10:1211–1220
43. Taylor RL (2022) Program FEAP, Ver. 8.6. University of California, Berkeley
44. Vu-Quoc L, Tan XG (2003) Optimal solid shells for non-linear analyses of multilayer composites. I. Statics. Comput Methods Appl Mech Eng 192:975–1016
45. Wagner W, Gruttmann F (2019) On a simple shell model for thin structures with functionally graded materials. In: Altenbach H et al (eds) Recent developments in the theory of shells, advanced structured materials, vol 110. Springer, Cham, pp 687–710
46. Wall WA, Bischoff M, Ramm E (2000) A deformation dependent stabilization technique, exemplified by EAS elements at large strains. Comput Methods Appl Mech Eng 188(4):859–871
47. Wilson EL, Taylor RL, Doherty WP, Ghaboussi J (1973) Incompatible displacement models. In: Fenves SJ, Perrone N, Robinson AR, Schnobrich WC (eds) Numerical and Computer Methods in Finite Element Analysis. Academic Press, New York, pp 43–57
48. Wisniewski K (2010) Finite Rotation Shells. Basic Equations and Finite Elements for Reissner Kinematics, CIMNE-Springer
49. Wisniewski K, Turska E (2009) Improved four-node Hu–Washizu elements based on skew coordinates. Computers & Structures 87:407–424
50. Wisniewski K, Turska E (2012) Four-node mixed Hu–Washizu shell element with drilling rotation. Int J Numer Methods Eng 90:506–536

51. Wisniewski K, Turska E (2018) Improved nine-node shell element MITC9i with reduced distortion sensitivity. Comput Mech 62:499–523
52. Wisniewski K, Turska E (2023) Reduced representations of assumed fields for Hu–Washizu solid-shell element. Comput Mech 71:957–990
53. Wisniewski K, Wagner W, Turska E, Gruttmann F (2010) Four-node Hu–Washizu elements based on skew coordinates and contravariant assumed strain. Comput Struct 88:1278–1284
54. Wriggers P (2008) Nonlinear finite element methods. Springer, Berlin
55. Wriggers P, Korelc J (1996) On enhanced strain methods for small and finite deformations of solids. Comput Mech 18(6):413–428
56. Wriggers P, Reese S (1996) A note on enhanced strain methods for large deformations. Comput Methods Appl Mech Eng 135(3–4):201–209
57. Zienkiewicz OC, Taylor RL (1989) The finite element method, vol 1. Basic formulation and linear problems, 4th edn. McGraw-Hill, London